Available online at www.sciencedirect.com
SCIENCE DIRECT®
Mechanics of Materials 37 (2005) 955–979
MECHANICS OF MATERIALS
www.elsevier.com/locate/mechmat

A continuum damage mechanics model for unidirectional composites undergoing interfacial debonding

P. Raghavan, S. Ghosh *

Department of Mechanical Engineering, The Ohio State University, Columbus, OH 43210, United States

Received 25 September 2003

Abstract

A continuum damage mechanics (CDM) model is developed in this paper for fiber reinforced composites with interfacial debonding. The model is constructed from rigorous micromechanical analysis of the Representative Volume Element (RVE) using the Voronoi cell FEM (VCFEM) that is followed by homogenizing microscopic variables using asymptotic homogenization. The microstructural damage mode considered in this paper is fiber–matrix interfacial debonding that is simulated using cohesive zone models in VCFEM. Following a systematic consideration of various order damage tensors, an anisotropic CDM model using fourth order damage tensor with stiffness characterized as an internal variable, is found to perform most accurately for this class of materials. The comparison of this CDM results with those obtained by homogenization of micromechanical analysis show excellent agreement between the two. Hence the CDM model is deemed suitable for implementing in macroscopic finite element codes to represent damage evolution in composites with significant efficiency.

Keywords: Cohesive zone model; Interfacial debonding; Voronoi cell FEM; Continuum damage mechanics; Homogenization

1. Introduction

Many composite materials exhibit non-uniformities at the microstructural level in the form of variations in fiber spacing, fiber size, shape, volume fraction and dispersion. Microstructural damage modes e.g. fiber cracking, interfacial decohesion or matrix cracking are sensitive to these local variations in morphological and constitutive parameters. Various phenomenological models have been proposed for failure prediction of these composites. However, many do not explicitly account for microstructural variabilities and their interaction. For example, failure surfaces that have been constructed from experimental

* Corresponding author. Tel.: +1 614 292 2599; fax: +1 614 292 7369.
E-mail address: ghosh.5@osu.edu (S. Ghosh).

0167-6636/$ - see front matter © 2005 Elsevier Ltd. All rights reserved.
doi:10.1016/j.mechmat.2004.10.003

observations to portray the locus of laminate failure under combined states of macroscopic stress in Feng (1991), Hashin (1980) and Tsai and Wu (1971) do not explicitly account for the microstructure and its evolution. Alternatively, macroscopic fracture mechanics theories have been applied to design composites, for which appropriate crack initiation and growth criteria have to be chosen from macroscopic experiments. A problem with many of these models is that the lack of underlying microstructure as well as damage mechanisms limit their applicability to different materials.

Micromechanical theories on the other hand solve boundary value problems of the Representative Volume Element (RVE) with microstructural distribution to predict constitutive response at the macroscopic level. Damage models for brittle materials with interacting microcracks have been proposed by Budiansky and O'Connell (1976), Benveniste (1983), Horii and Nemat-Nasser (1987) and others. Numerical micromechanical models using high resolution mesh for the microstructure have been used more recently to generate stress–strain patterns in evolving microstructures. Unit cell models using cohesive zone models, for modeling the inception and progress of interfacial decohesion, have been proposed in Camacho and Ortiz (1996), Needleman (1990) and Tvergaard (1995). These analyses have provided important insight into the microstructure damaging process. However, the uniformity assumptions to curtail computational efforts in some cases are restrictive, especially since the damage process is sensitive to the local distribution. Also, in most engineering analysis and design problems, it is impossible to conduct detailed micromechanical analysis for a full structural component. In these analyses, it is convenient to use macroscopic constitutive laws obtained by the homogenization of variables obtained from micromechanics simulations. The development of continuum damage mechanics models from rigorous micromechanical simulations appears promising in this regard.

Continuum Damage Mechanics (CDM), developed in the last few decades, provides a framework for incorporating the effects of damage induced stiffness softening, anisotropy etc. in constitutive equations. Damage variables in these models are represented by tensors of varying orders (e.g. scalars, vectors or tensors) with their evolution defined from experimental observations. Phenomenological CDM models, originally proposed by Kachanov (1987), have been used extensively for modeling creep and fatigue damage by several authors as described in Lemaitre and Chaboche (1990), Krajicinovic (1996) and Voyiadjis and Kattan (1999). A number of these models represent damage as a scalar variable in the context of 'scalar damage models'. Chaboche (1981) has proposed a thermodynamic framework for CDM for isotropic damage. However, Chow and Wang (1987) have shown even for an initially isotropic material, experimental results point to anisotropic damage development in aluminum alloys. Generalizations of the CDM to orthotropic damage models using vectors has been proposed by Krajicinovic and Fonseka (1981). The models have been used to analyze damage in sheet metal forming process by Zhu and Cescotto (1995). Talreja (1990) have used a second order tensor field to describe damage and developed a phenomenological constitutive theory for composite laminates. Voyiadjis and Kattan (1999) have used the orthotropic damage to model matrix cracking and interfacial debonding in fiber reinforced composites. The limitations of the widely used second order damage model in manifesting general damage have been discussed in Carol et al. (1994). Fully anisotropic damage models with fourth order damage tensors based on principles of thermodynamics, have been proposed by Lemaitre and Chaboche (1990), Ortiz (1985) for damage in concrete, Simo and Ju (1987) for damage coupled with elasto-plasticity in concrete. These phenomenological models however do not include microstructural features like morphology and microstructural evolution.

A few micromechanical damage modeling approaches have involved averaging over the microstructural RVE for evaluating macroscopic damage (e.g. Nemat-Nasser and Hori, 1999). Lene and Leguillon (1982) have assumed a tangential slip at the fiber/matrix interface of the RVE and used asymptotic homogenization method to obtain macroscopic damaged stiffness of the composite material. Choi and Tamma (2001a,b) have used the second order damage model of Chow and

Wang (1987), to predict macro crack initiation loads for woven fabric composites. Macroscopic damage parameters are generated by averaging micromechanical variables obtained from micromechanical damage analysis with the stiffness degradation method. Fish et al. (1999) have used two-scale asymptotic homogenization with a position dependent microscopic scalar damage parameter to represent cracking in matrix, which is assumed to evolve with strain. The homogenization method with its RVE-based computations at each integration point of the macroscopic model, makes this a computationally expensive process, even though it is effective in characterizing damage.

This paper is aimed at developing a continuum damage model for composite materials with non-uniform microstructures from detailed micromechanical analysis of damage. It is assumed that a RVE may be assumed with reasonable confidence for these analyses. Interfacial debonding between matrix and inclusion phases of the microstructure is considered as the damage mode in this paper. Interfacial debonding is simulated using cohesive zone models. The micromechanical analyses in each RVE are conducted with the Voronoi cell finite element model (Ghosh et al., 2000; Moorthy and Ghosh, 2000), in which cohesive zone models are used to model interfacial debonding. The asymptotic homogenization method (Ghosh et al., 1995; Ghosh et al., 2001) is used to evaluate macroscopic damage variables and their evolution laws. Rigorous comparison of the isotropic, orthotropic and anisotropic continuum damage mechanics models are made with averaged micromechanics predictions to examine their validity for the class of composites considered. Based on the effectiveness of the anisotropic models, the strain based anisotropic damage model developed in Simo and Ju (1987) is modified for damage in anisotropic composite materials. Parameters which characterize anisotropic stiffness degradation are found to vary with evolution of microstructural state variables. Consequently, a set of macroscopic strain paths is chosen, along which anisotropic parameters are evaluated. Numerical examples are conducted for demonstrating the effectiveness of the CDM model in predicting damage in composite structures.

2. The voronoi cell FEM for microstructures with interfacial debonding

The Voronoi Cell finite element model (VCFEM) has been developed by Ghosh et al. (2000), Moorthy and Ghosh (2000), Li and Ghosh (under review) and Moorthy and Ghosh (1996) for analyzing stresses and strains in heterogeneous microstructures of composite and porous materials. In this model, heterogeneity based Dirichlet tessellation of non-uniform microstructural regions yields the unstructured Ghosh and Mukhopadhyay (1991) for microstructural analysis, as shown in Fig. 14a. The Voronoi cell FEM, in which each element in VCFEM consists of a heterogeneity and its immediate surrounding matrix, has been developed as an efficient tool VCFEM for problems with evolving microstructures. Micromechanics problems of elastic–plastic composites and porous media with evolving damage by particle cracking have been solved in Moorthy and Ghosh (2000, 1996), while and elastic composites with interfacial debonding induced damage have been analyzed in Ghosh et al. (2000). In the latter work, the VCFEM is coupled with cohesive zone models to depict interfacial debonding as a phenomenon of progressive separation across an extended crack tip or cohesive zone that is resisted by cohesive tractions. A summary of the model developed in Ghosh et al. (2000) is given next.

Consider a heterogeneous microstructural domain Ω consisting of N inclusions each contained in a Voronoi cell element Ω_e, as shown in Fig. 1a. The matrix and the reinforcement phases in each element are denoted by Ω_m and Ω_c respectively, i.e. $\Omega_e = \Omega_m \cup \Omega_c$. Each element boundary $\partial\Omega_e$ is assumed to be comprised of the prescribed traction and displacement boundaries $\partial\Gamma_{tm}$ and $\partial\Gamma_{um}$ respectively, and the inter-element boundary $\partial\Gamma_m$, i.e. $\partial\Omega_e = \partial\Gamma_{tm} \cup \partial\Gamma_{um} \cup \partial\Gamma_m$. For allowing decohesion of the matrix-inclusion interface, an incompatible displacement field is facilitated across the interface through a set of connected node-pairs. The nodes in each pair belong to the matrix and inclusion boundaries $\partial\Omega_c^m$ and $\partial\Omega_c^c$, respectively. $\partial\Omega_c^c$ has an outward normal $\mathbf{n}^c$ ($=\mathbf{n}^m$), while $\mathbf{n}^e$ is the outward normal to $\partial\Omega_e$. It should be noted that the interfacial zone has zero

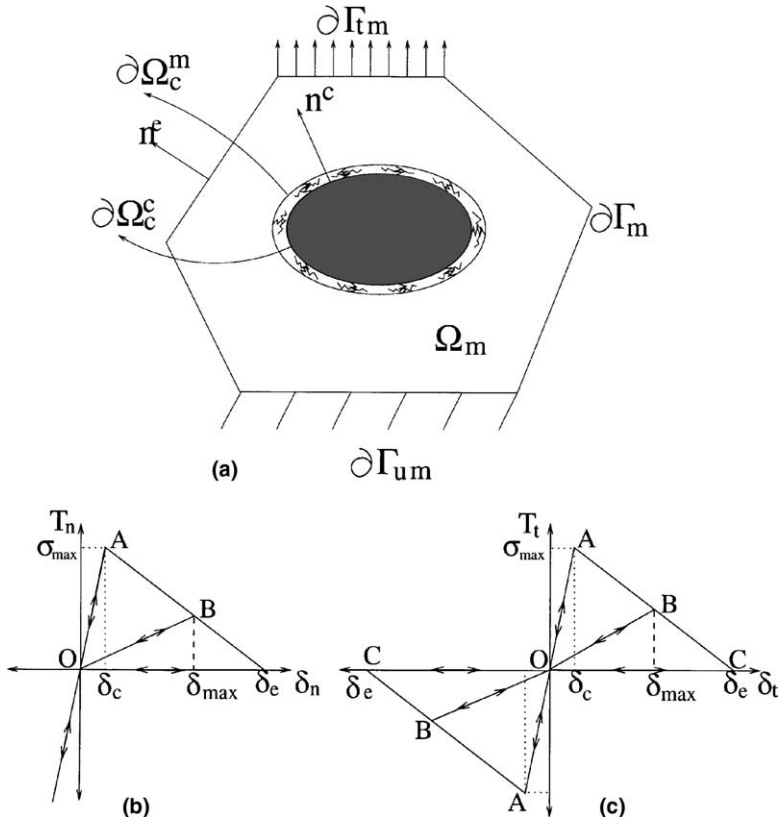

Fig. 1. Voronoi cell finite element with fiber–matrix interface modeled using nonlinear springs: (a) normal and (b) tangential traction–displacement behavior for a bilinear cohesive zone model.

thickness prior to deformation, but nodes may separate with progression of deformation and onset of decohesion.

An assumed stress hybrid formulation is adopted in VCFEM (Ghosh et al., 2000; Moorthy and Ghosh, 2000; Moorthy and Ghosh, 1996). In this formulation, special assumptions are made for interpolation of equilibriated stress fields in the matrix and fiber phases from considerations of known micromechanics solutions. Additionally, assumptions on compatible displacement fields are also made on the element boundary and matrix–fiber interface. In the incremental formulation for accommodating evolving interfacial damage with changing applied loads, deformation and stress fields, a complementary energy functional is expressed for each element in terms of increments of stress and displacement fields as

$$
\begin{aligned}
&\Pi_e(\sigma,\Delta\sigma,u,\Delta u)\\
&\quad=-\int_{\Omega_m}\Delta B(\sigma^m,\Delta\sigma^m)\mathrm{d}\Omega-\int_{\Omega_c}\Delta B(\sigma^c,\Delta\sigma^c)\mathrm{d}\Omega\\
&\qquad-\int_{\Omega_m}\epsilon^m:\Delta\sigma^m\,\mathrm{d}\Omega-\int_{\Omega_e}\epsilon^c:\Delta\sigma^c\,\mathrm{d}\Omega\\
&\qquad+\int_{\partial\Omega_e}(\sigma^m+\Delta\sigma^m)\cdot n^e\cdot(u^m+\Delta u^m)\mathrm{d}\partial\Omega\\
&\qquad-\int_{\partial\Gamma_{tm}}(\bar{t}+\Delta\bar{t})\cdot(u^m+\Delta^m)\mathrm{d}\Gamma\\
&\qquad+\int_{\partial\Omega_m^c}(\sigma^m+\Delta\sigma^m)\cdot n^c\cdot(u^m+\Delta u^m)\mathrm{d}\partial\Omega\\
&\qquad+\int_{\partial\Omega_c^c}(\sigma^c+\Delta\sigma^c)\cdot n^c\cdot(u^c+\Delta u^c)\mathrm{d}\partial\Omega\\
&\qquad-\int_{\partial\Omega_m^e/\partial\Omega_c^e}\int_{u_n^m-u_n^c}^{u_n^m+\Delta u_n^m-u_n^c+\Delta u_n^c}T_n d(u_n^m-u_n^c)\mathrm{d}\partial\Omega
\end{aligned}
$$

$$-\int_{\partial\Omega_m^e/\partial\Omega_c^e}\int_{u_t^m-u_t^c}^{u_t^m+\Delta u_t^m-u_t^c+\Delta u_t^c} T_t d(u_t^m-u_t^c)\mathrm{d}\partial\Omega \tag{1}$$

where B is the complementary energy density and the superscripts m and c correspond to variables associated with the matrix and inclusion phases. $\boldsymbol{\sigma}^m$ and $\boldsymbol{\sigma}^c$ are the equilibriated stress fields, $\boldsymbol{\epsilon}^m$ and $\boldsymbol{\epsilon}^c$ the corresponding strain fields in different phases of each Voronoi element. Also, $\mathbf{u}$, $\mathbf{u}^m$ and $\mathbf{u}^c$ are the kinematically admissible displacement fields on $\partial\Omega_e$, $\partial\Omega_c^m$ and $\partial\Omega_c^c$ respectively. The prefix Δ corresponds to increments. The last two terms provide the work done by the interfacial tractions $\mathbf{T}^m = T_n^m\mathbf{n}^m + T_t^m\mathbf{t}^m$ due to interfacial separation $(\mathbf{u}^m - \mathbf{u}^c)$, where T_n and T_t are the normal and tangential components that are described by cohesive laws. The total energy for the entire heterogeneous domain is obtained by adding the energy functionals for N elements as

$$\Pi = \sum_{e=1}^{N}\Pi_e \tag{2}$$

Independent assumptions on stress increments $\Delta\boldsymbol{\sigma}$ are made in each of the element phases to accommodate stress jumps across the interface. A convenient method of deriving equilibriated stress increments in each phase is through the introduction of stress functions $\boldsymbol{\Phi}(x, y)$, e.g. Airys stress function in 2D. Important micromechanics observations, that interfacial stress concentrations depend on the shape of the heterogeneity, have been incorporated in the choice of stress functions in Ghosh et al. (2000) and Moorthy and Ghosh (2000) through the decomposition of the stress functions into (a) a purely polynomial function $\boldsymbol{\Phi}_{\text{poly}}$ and (b) a *reciprocal* function $\boldsymbol{\Phi}_{\text{rec}}$ ($\boldsymbol{\Phi} = \boldsymbol{\Phi}_{\text{poly}} + \boldsymbol{\Phi}_{\text{rec}}$). The reciprocal terms are used for accurate stress concentrations near the interface. Stress increments in the matrix and inclusion phases of Voronoi cell elements are finally obtained by differentiating the stress functions to yield expressions of the form:

$$\begin{aligned}&\{\Delta\sigma^m\} = [\mathbf{P}^m]\{\Delta\boldsymbol{\beta}^m\} \quad \text{and}\\ &\{\Delta\sigma^c\} = [\mathbf{P}^c]\{\Delta\boldsymbol{\beta}^c\}\end{aligned} \tag{3}$$

where $[\mathbf{P}^m]$ and $[\mathbf{P}^c]$ are the stress interpolation matrices. The boundary displacements are generated by interpolation in terms of nodal displacements on $\partial\Omega_e$, $\partial\Omega_m^c$ and $\partial\Omega_c^c$ using conventional linear or quadratic shape functions.

$$\begin{aligned}&\{\Delta\mathbf{u}\} = [\mathbf{L}^e]\{\Delta\mathbf{q}\} \quad \text{on } \partial\Omega_e\\ &\{\Delta\mathbf{u}^m\} = [\mathbf{L}^c]\{\Delta\mathbf{q}^m\} \quad \text{on } \partial\Omega_m^c\\ &\text{and}\\ &\{\Delta\mathbf{u}^c\} = [\mathbf{L}^c]\{\Delta\mathbf{q}^c\} \quad \text{on } \partial\Omega_c^c\end{aligned} \tag{4}$$

where $\{\Delta\mathbf{q}\}$, $\{\Delta\mathbf{q}^m\}$ and $\{\Delta q^c\}$ are the generalized nodal displacement vectors. The stress and displacement interpolations are substituted in Eqs. (1) and (2). Subsequently stationary conditions of these equations are evaluated with respect to the stress parameters $\Delta\boldsymbol{\beta}^m$ and $\Delta\boldsymbol{\beta}^c$, and displacement parameters $\{\Delta q\}$, $\{\Delta\mathbf{q}^m\}$ and $\{\Delta\mathbf{q}^c\}$ to yield the stress and displacement solutions in each element. Details of VCFEM formulation and solution methodology are presented in Ghosh et al. (2000) and Moorthy and Ghosh (2000).

The interfacial traction components (T_n, T_t) in the energy functional Eq. (1) are related to the interfacial separation δ_n $(= u_n^m - u_n^c)$, δ_t $(= u_t^m - u_t^c)$ using cohesive laws that govern nonlinear interfacial springs along the normal and tangential directions. In these laws, tractions across the interface reach a maximum, subsequently decrease and eventually vanish with the increasing displacement jump. A number of cohesive zone models have been provided by various authors (Camacho and Ortiz, 1996; Chandra et al., 2002; Geubelle, 1995; Needleman, 1992; Ortiz and Pandolfi, 1999). A bilinear cohesive zone model, postulated by Ortiz and Pandolfi (1999), is used in this work to represent interfacial debonding. In this model, a relation between the effective traction t $(= \sqrt{T_n^2 + T_t^2})$ and the effective displacement jump δ $(= \sqrt{\delta_n^2 + \beta^2\delta_t^2})$ is expressed through a free energy potential ϕ as

$$t = \frac{\partial\phi(\delta)}{\partial\delta} \tag{5}$$

where δ_n and δ_t are displacement jumps in the normal and tangential directions respectively.

The factor β is introduced to provide different weights to normal and tangential displacements. The t–δ relation in the bilinear model is expressed as (Ortiz and Pandolfi, 1999)

$$t = \begin{cases} \dfrac{\sigma_{\max}}{\delta_c}\delta & \text{if } \delta \leqslant \delta_c \text{ (hardening domain)} \\ \dfrac{\sigma_{\max}}{\delta_c - \delta_e}(\delta - \delta_e) & \text{if } \delta_c < \delta \leqslant \delta_e \text{ (softening domain)} \\ 0 & \text{if } \delta > \delta_e \text{ (complete debonding)} \end{cases} \tag{6}$$

from which the normal and tangential tractions are derived as

$$\begin{aligned} T_n &= \frac{\partial \phi}{\partial \delta_n} = \frac{\partial \phi}{\partial \delta}\frac{\partial \delta}{\partial \delta_n} \\ &= \begin{cases} \dfrac{\sigma_{\max}}{\delta_c}\delta_n & \text{if } \delta \leqslant \delta_c \\ \dfrac{\sigma_{\max}}{\delta}\dfrac{\delta - \delta_e}{\delta_c - \delta_e}\delta_n & \text{if } \delta_c < \delta \leqslant \delta_e \\ 0 & \text{if } \delta > \delta_e \end{cases} \\ T_t &= \frac{\partial \phi}{\partial \delta_t} = \frac{\partial \phi}{\partial \delta}\frac{\partial \delta}{\partial \delta_t} \\ &= \begin{cases} \dfrac{\sigma_{\max}}{\delta_c}\beta^2\delta_t & \text{if } \delta < \delta_c \\ \dfrac{\sigma_{\max}}{\delta}\dfrac{\delta - \delta_e}{\delta_c - \delta_e}\beta^2\delta_t & \text{if } \delta_c < \delta \leqslant \delta_e \\ 0 & \text{if } \delta > \delta_e \end{cases} \end{aligned} \tag{7}$$

Fig. 1b and c show the normal traction–separation response for $\delta_t = 0$ and tangential traction–separation response for $\delta_n = 0$ respectively. When the normal displacement δ_n is positive, the traction at the interface increases linearly to a maximum value of $\sigma_{\max}$ (point A) corresponding to a value of δ_c before it starts decreasing to zero at a value of δ_e (point C). The unloading behavior in the hardening region is linear following the loading path. In the softening region, the unloading proceeds along a different linear path from the current position to the origin with a reduced stiffness. This is shown by the line BO in Fig. 1b and c, for which the t–δ relation is

$$t = \frac{\sigma_{\max}}{\delta_{\max}}\frac{\delta_{\max} - \delta_e}{\delta_c - \delta_e}\delta \qquad \delta_c < \delta_{\max} < \delta_e \text{ and } \delta < \delta_{\max} \tag{8}$$

Both normal and tangential tractions vanish when $\delta > \delta_e$. Reloading follows the path OBC demonstrating the irreversible nature of the damage process. The magnitudes of the tangential traction–displacement relation are independent of the sign, and hence the behavior is same for δ_t positive and negative. When the normal displacement is negative in compression, stiff penalty springs with high stiffnesses are introduced between the node-pairs at the interface.

3. Homogenization for macroscopic variables and properties

Multi-scale models require the evaluation of homogenized or effective material properties and macroscopic variables like stresses and strains. In Ghosh et al. (1995), Ghosh et al. (2001) and Raghavan et al. (2001), the asymptotic homogenization method has been used along with periodicity assumptions over the microstructural RVE, for evaluating effective properties by averaging variables over the RVE. A majority of analyses in the literature (e.g. Fish et al., 1999; Lene and Leguillon, 1982; Yuan et al., 1997) have considered a rectangular array of fiber in the microstructure, resulting in a rectangular RVE containing a single fiber. Determination of the statistically equivalent RVE is considerably more difficult for non-uniform microstructures. Methods for determining statistically equivalent RVEs for non-uniform microstructures by using statistical functions have been discussed in Pyrz (1994a,b), Raghavan and Ghosh (2004) and Raghavan et al. (2001). Bulsara et al. (1999) have studied the effect of RVE size on damage initiation due to debonding and matrix cracking for non-uniform microstructures.

The asymptotic homogenization method (Raghavan and Ghosh, 2004; Raghavan et al., 2001), in conjunction with detailed micromechanical analysis by VCFEM, is adopted in this work to obtain homogenized properties and averaged variables. Assuming variables exhibit periodic behavior in the RVE, the or averaged stress–strain relation for a heterogeneous elastic material takes the form

$$\bar{\sigma}_{ij} = E^H_{ijmn}\bar{\epsilon}_{mn} \tag{9}$$

Here $\bar{\sigma}_{ij}$ is a volume averaged stress obtained by integrating the VCFEM generated microstructural stress in the RVE, using the formula

$$\bar{\sigma}_{ij} = \frac{1}{Y}\int_Y \sigma_{ij}(Y)\,\mathrm{d}Y \tag{10}$$

where Y is the RVE domain. Similarly, the volume averaged macroscopic strain is generated using the formula

$$\begin{aligned}\bar{\epsilon}_{ij} &= \frac{1}{Y}\int_Y \epsilon_{ij}(Y)\,\mathrm{d}Y \\ &= \frac{1}{Y}\left[\int_{Y_m}\epsilon_{ij}(Y)\,\mathrm{d}Y + \int_{Y_c}\epsilon_{ij}(Y)\,\mathrm{d}Y \right. \\ &\quad \left. + \int_{Y_{\text{interface}}}\epsilon_{ij}(Y)\,\mathrm{d}Y\right]\end{aligned} \tag{11}$$

Y_m, Y_c and $Y_{\text{interface}}$ in the above equation correspond to the matrix, inclusion and interface domains in the RVE respectively. By applying divergence theorem to the last term in Eq. (11), the average strain may be derived as

$$\bar{\epsilon}_{ij} = \frac{1}{Y}\int_Y \epsilon_{ij}(Y)\,\mathrm{d}Y + \frac{1}{2Y}\int_{\partial\Omega^e_m/\partial\Omega^e_c}([u_i]n_j + [u_j]n_i)\mathrm{d}S \tag{12}$$

where $[u_i]$ denotes the jump in the displacement components across the fiber–matrix interface with outward normal n_i. This integral is evaluated over all the fiber–matrix interfaces in the RVE i.e. $\bigcup \Omega^e_m/\partial\Omega^e_c$. The additional term in strain averaging due to imperfect interface has been suggested by Lissenden and Herakovich (1995) and Nemat-Nasser and Hori (1999). For perfect interfaces the displacement jump $[u_i]$ is zero resulting in the vanishing of this correction term.

In the present analysis, the homogenized properties with the elasticity tensor E^H_{ijkl} are assumed to be orthotropic. For plane strain problems, the components of E^H_{ijkl} are calculated by solution of three separate boundary value problems of the entire RVE. The loading in each of these problems is in the form of imposed unit macroscopic strains $e_{ij} = \frac{1}{2}(\frac{\partial u_i}{\partial x_j} + \frac{\partial u_j}{\partial x_i})$, stated as

$$\begin{Bmatrix} e_{xx} \\ e_{yy} \\ e_{xy} \end{Bmatrix}^{\mathrm{I}} = \begin{Bmatrix} 1 \\ 0 \\ 0 \end{Bmatrix}, \quad \begin{Bmatrix} e_{xx} \\ e_{yy} \\ e_{xy} \end{Bmatrix}^{\mathrm{II}} = \begin{Bmatrix} 0 \\ 1 \\ 0 \end{Bmatrix}$$
$$\begin{Bmatrix} e_{xx} \\ e_{yy} \\ e_{xy} \end{Bmatrix}^{\mathrm{III}} = \begin{Bmatrix} 0 \\ 0 \\ 1 \end{Bmatrix} \tag{13}$$

In each problem the strain in the fiber direction is set to zero, i.e. $e_{zz} = 0$. Additionally, the periodicity on RVE boundaries implies that all points on the boundary are constrained to displace periodically. For nodes on the boundary which are separated by the periods Y_1, Y_2, Y_3 along one or more coordinate directions, the displacement constraints may be expressed as one of the following

$$u_i(x_1, x_2, x_3) = u_i(x_1 \pm k_1 Y_1, x_2 \pm k_2 Y_2, x_3 \pm k_3 Y_3) \quad i = 1, 2, 3 \tag{14}$$

where k_1, k_2, k_3 may assume the values 0 or 1, depending on the node locations. The homogenized elastic stiffness components E^H_{1111}, E^H_{2222}, E^H_{1212}, E^H_{1133}, E^H_{2233} and E^H_{1122} are calculated from the volume averaged stresses Σ_{ij} in Eq. (10). To calculate the effective property along the fiber direction, a fourth boundary value problem with $(\bar{\epsilon}_{xx}, \bar{\epsilon}_{yy}, \bar{\epsilon}_{xy}, \bar{\epsilon}_{zz})^{\mathrm{T}} = (0, 0, 0, 1)^{\mathrm{T}}$ needs to be solved. The macroscopic orthotropic elastic constants like Young's moduli (E_1, E_2, E_3), Shear modulus (G_{12}) and Poisson's ratio (ν_{12}, ν_{13}, ν_{23}) can be obtained from inverse relations of E^H_{ijkl}.

3.1. Numerical examples on homogenized properties with imperfect interfaces

Two numerical examples, involving homogenization of variables obtained by micromechanical VCFEM analysis of heterogeneous RVEs with imperfect interfaces, are considered in this section. The examples are chosen to validate the methods of evaluating effective material properties with VCFEM-based micromechanical analyses. In the first example, a square RVE containing a single circular fiber with an imperfect interface is considered. This problem, representing a uniformly distributed microstructure has been analyzed by Yuan et al. (1997) using the commercial ANSYS

software. The interface in this example is assumed to be partially bonded after a steady state has been attained, i.e. no crack propagation is considered. In VCFEM, the debonded portion of the interface is modeled with springs of zero stiffness, while stiff springs are used to represent the intact regions. The fiber volume fraction in this composite is 40%. The matrix material is 1723 Glass with Young's modulus, $E_m = 88$ GPa and Poisson's ratio, $v_m = 0.2987$, whereas the fiber is Nicalon with Young's modulus, $E_f = 200$ GPa and Poisson's ratio $v_f = 0.2222$. The effective elastic moduli are evaluated for different values of the debonded semi-angle α (see Fig. 2), ranging from $\alpha = 0°$ (composite with perfect interface) to $\alpha = 90°$ (completely debonded composite). Symmetric debonding about the x and y axes are assumed in this example.

Excellent agreement with results in Yuan et al. (1997) are shown in Fig. 2a and b for Young's/shear moduli Poissons ratio respectively. While Young's moduli and the shear modulus reduce monotonically with increasing α, the same is not the case with Poisson's ratio v_{12}, which reaches a minimum around 68° and then increases back again. The modulus along the fiber direction E_3 is found to be insensitive to the debonding angle.

The second example is intended to understand the effect of progressively increasing debonding on the macroscopic behavior of the composite. The RVE considered is once again a square domain with a single circular fiber with a volume fraction of 20%. The matrix material is has Young's modulus, $E_m = 4.6$ GPa and Poisson's ratio, $v_m = 0.4$, while the fiber material has a Young's modulus $E_f = 210$ GPa and Poisson's ratio, $v_f = 0.3$. The cohesive law parameters for the interface are $\sigma_m = 0.02$ GPa, $\delta_c = 5.0 \times 10^{-5}$ m and $\delta_e = 20 \times 10^{-4}$ m. Fig. 3a shows the macroscopic or averaged stress–strain curve along the loading

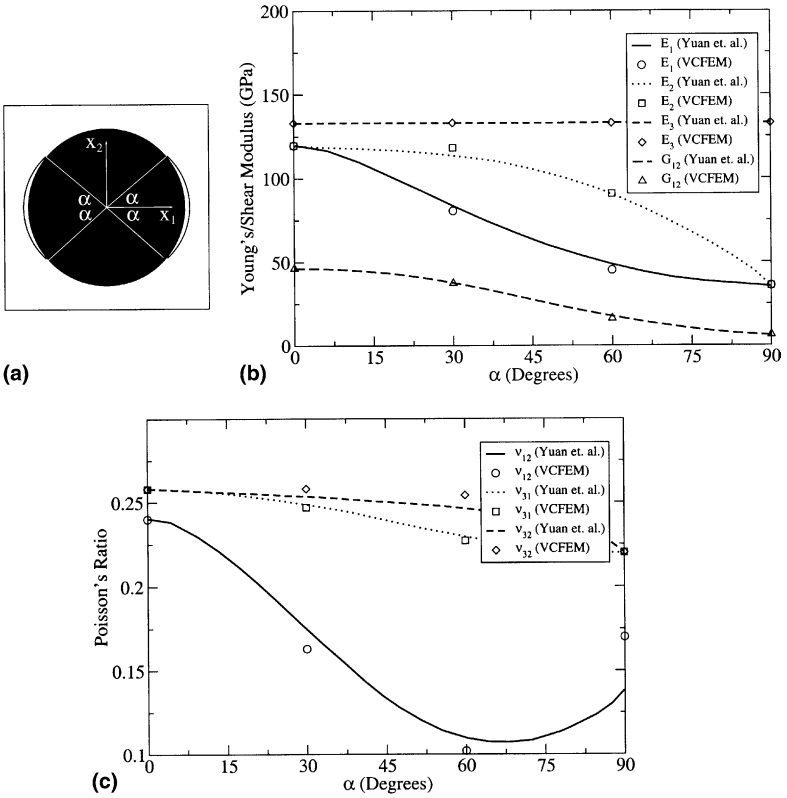

Fig. 2. (a) RVE with pre-described debonding angles α, comparison of effective properties; (b) Young's/shear modulus and (c) Poisson's ratio obtained using VCFEM with those of Yuan et al. (1997).

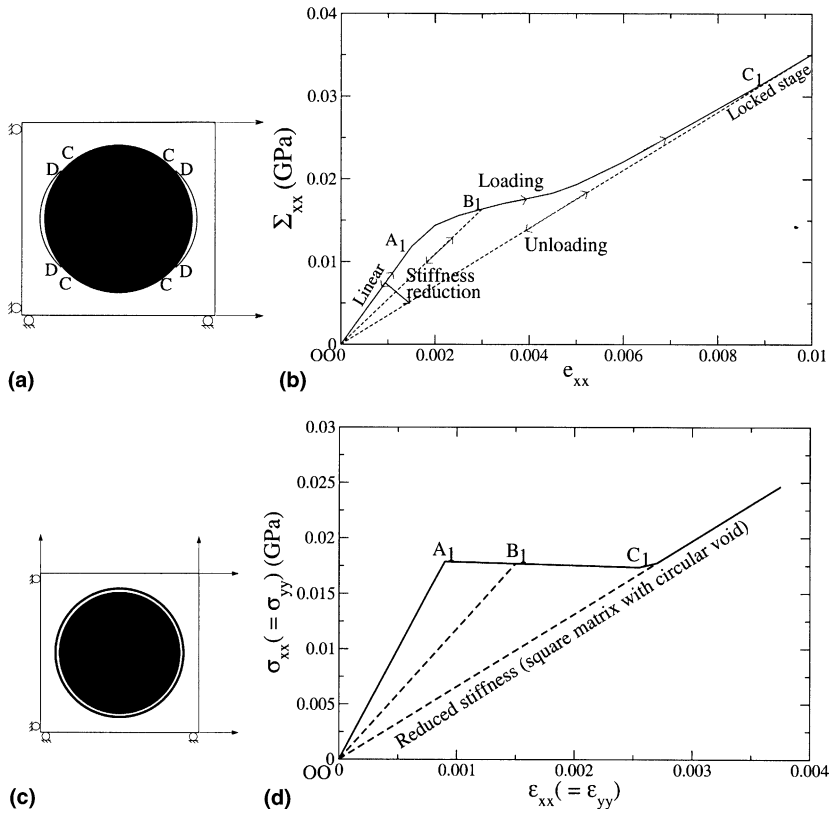

Fig. 3. RVE subjected to loading in (a) simple tension and (c) biaxial tension. Macroscopic stress–strain curve for the RVE loaded in (b) simple tension and (d) biaxial tension.

direction corresponding to simple tension loading. Three distinct regions emerge in this figure with increased loading. They are: (a) linear region from 0 till A_1 corresponding to a bonded interface with $\delta_n \leqslant \delta_c$; (b) a nonlinear region from A_1 to C_1 corresponding to softening and subsequent debonding with $\delta_n \delta_c$; and (c) a linear region beyond C_1 indicating that no further softening or debonding can take place for any additional external loading. Unloading from any point in the nonlinear stage results in a linear stress–strain behavior with no residual stress or strain at O, as shown by the line B_1–O. Reloading causes the stress–strain behavior to follow the path O–B_1–C_1. This is consistent with the cohesive law in Fig. 1b and c, where unloading/reloading path during softening follows the path O–B–C. Unloading from beyond C_1 follows a linear path to the origin. As seen in Fig. 3a, the debonding is symmetric about the mid-plane and the top and bottom of the interface are in states of compression (C–C in Fig. 3a inset). This prevents further debonding of the interface loading to a constant post-debonding macroscopic stiffness. For the example with biaxial loading as shown in Fig. 3b, there is complete debonding of the interface. This results in a voided material-like behavior of the composite with a significantly reduced post-debonding stiffness. This exercise lays the foundation for a robust continuum damage mechanics model that is developed in this work from detailed micromechanical analyses.

4. A continuum damage mechanics model from VCFEM-based micromechanical analysis

In continuum damage mechanics (CDM), macroscopic constitutive models involving

macroscopic internal variables are used to represent material behavior with evolving micro-defects or micro-damage. The set of internal variables typically chosen are scalar, second order tensor or fourth order tensor leading to the so-called scalar isotropic, orthotropic and anisotropic damage models. Each of these model categories is studied in this section, in an effort to develop a debonding-induced damage evolution model for non-uniform composites. The capabilities and limitations of these models are examined for multi-axial loading conditions.

The general form of CDM models (Kachanov, 1987) introduce a fictitious effective stress $\tilde{\sigma}_{ij}$ acting on an effective resisting area ($\tilde{A}$), which is caused by reduction of the original resisting area A due to material degradation caused by the presence of microcracks and stress concentration in the vicinity of cracks. The effective stress is related to the actual Cauchy stress σ_{ij} in the damaged material using the fourth order damage effect tensor M_{ijkl} as

$$\tilde{\sigma}_{ij} = M_{ijkl}(D_{ijkl})\sigma_{kl} \tag{15}$$

where D_{ijkl} is the damage tensor, can be of zeroth, second or fourth order, depending on the model employed. Different hypotheses based on equivalence of strain or elastic energy have been proposed to evaluate M_{ijkl} and hence establish a relation between the damaged and undamaged stiffnesses. Lemaitre and Chaboche (1990) have proposed the equivalent strain hypothesis in which the fictitious stress $\tilde{\sigma}_{ij}$, when applied to the undamaged material element produces the same strain state as that by the actual stress σ_{ij}, applied to the damaged material. It has been noted in Hansen and Schreyer (1994) and Simo and Ju (1987) that the strain equivalence assumption for higher dimensions leads to a non-symmetric stiffness matrix. Alternatively, the hypothesis of equivalent elastic energy has been proposed by Cordebois and Sidoroff (1982), in which the elastic energy for a damaged material with the actual stress is assumed to be equivalent in form to that of the undamaged material with the fictitious effective stress. This principle has been used in the damage modeling of Chow and Wang (1987), Zhu and Cescotto (1995) and Voyiadjis and Kattan (1999) and others and will be pursued in this work. The equivalence is established by equating the elastic energy in the damaged state to that in a hypothetical undamaged state as

$$\begin{aligned} W(\sigma, D) &= \frac{1}{2}\sigma_{ij}(E_{ijkl}(D))^{-1}\sigma_{kl} \\ &= W(\tilde{\sigma}, 0) = \frac{1}{2}\tilde{\sigma}_{ij}(E^0_{ijkl})^{-1}\tilde{\sigma}_{kl} \end{aligned} \tag{16}$$

Here E^0_{ijkl} is the initial undamaged stiffness and $E_{ijkl}(D)$ is the stiffness of the damaged material. Substituting Eq. (15) in Eq. (16), the relation between the damaged and undamaged stiffnesses is established as

$$E_{ijkl} = (M_{pqij})^{-1}E^0_{pqrs}(M_{rskl})^{-1} \tag{17}$$

With an appropriate choice of the order of the damage tensor and the assumption of a function for M_{ijkl}, Eq. (17) can be used to formulate a damage evolution model using micromechanics and homogenization.

4.1. Isotropic damage model with scalar variable

The isotropic damage models with scalar damage was proposed by Kachanov (1987) and have been used by Simo and Ju (1987), Hansen and Schreyer (1994) and Lemaitre and Chaboche (1990) for modeling damage in concrete, metals etc. The tensor M_{ijkl} in this model is written as

$$M_{ijkl} = \frac{1}{2(1-D)}(\delta_{ik}\delta_{jl} + \delta_{il}\delta_{jk}) \tag{18}$$

where D is the scalar damage variable. Using Eq. (17), the damaged stiffness with all symmetries retained, can be expressed as

$$E_{ijkl} = (1-D)^2 E^0_{ijkl} \tag{19}$$

In two dimensional plane strain analyses, the stiffness matrix is expressed as

$$\begin{bmatrix} E_{1111} & E_{1122} & E_{1112} & E_{1133} \\ E_{2211} & E_{2222} & E_{2212} & E_{2233} \\ E_{1211} & E_{1222} & E_{1212} & E_{1233} \\ E_{3311} & E_{3322} & E_{3312} & E_{3333} \end{bmatrix}$$

The square RVE shown in Fig. 3 is considered again for examining the validity of the scalar damage law for composites with interfacial debonding.

In this example, the RVE subjected to simple tension loading in the horizontal (x) direction is micromechanically analyzed by VCFEM using the properties discussed in the second example of Section 3.1. Interfacial debonding initiates at the poles (intersection with the x axis) of the inclusion and propagates in the vertical direction in a symmetric manner about the x and y axes. However Poisson's effect causes the top and bottom poles and their neighboring regions of the interface to be in compression and hence this region remains bonded at all loads as shown in Fig. 3a inset. Homogenization of the micromechanics variables by the method discussed in Section 3.1 is conducted, for the configuration when the debonding process has arrested and when the RVE evolution has attained a locked position. The homogenized pre- and post-damaged stiffness coefficients in the x–y coordinate system are as follows:

Undamaged stiffness E^0_{ijkl} in GPa

$$\begin{bmatrix} 12.39 & 7.60 & 0 & 7.55 \\ 7.60 & 12.39 & 0 & 7.55 \\ 0 & 0 & 2.16 & 0 \\ 7.55 & 7.55 & 0 & 51.39 \end{bmatrix}$$

$\Rightarrow$ Damaged stiffness E_{ijkl} in GPa

$$\begin{bmatrix} 4.64 & 2.90 & 0 & 2.98 \\ 2.90 & 6.76 & 0 & 2.98 \\ 0 & 0 & 1.00 & 0 \\ 2.98 & 2.98 & 0 & 48.32 \end{bmatrix}$$

The homogenized results show that while the pre-damage orthotropy is retained in the post-damaged stiffness, the stiffness coefficients do not scale down uniformly with evolving damage. Due to compressive stress along the top and bottom regions of the interface (near north and south poles) and debonding along the two sides (east and west poles) of the interface, the coefficient E_{2222} is stiffer than E_{1111}. The scalar damage model is incapable of predicting this type of stiffness degradation since it assumes uniform damage development in all directions. Such observations have also been made by Chow and Wang (1987) whose experiments on initially isotropic aluminum alloy showed that experimental damage along the loading direction was more pronounced than that in the transverse direction.

4.2. Orthotropic damage model with second order tensor variables

Orthotropic damage models using second order symmetric damage tensor were proposed by Cordebois and Sidoroff (1982) and have been developed and used by many authors to account for anisotropic material degration. Chow and Wang (1987) have used a new the damage effect tensor to study damage in aluminum. Zhu and Cescotto (1995) have used this model to describe elasto-visco-plastic damage model for sheet forming process. Park and Voyiadjis (1997) have used the second order damage model for describing nucleation and growth of voids in the matrix, fracture of fibers, debonding and delamination in composites. In these models, the components of a second order symmetric damage tensor are expressed as $D_{ij} = D_{ji}\ \forall i, j = 1, 2, 3$. The damage effect tensor can then be described by incorporating the second order damage tensor in Eq. (18) as

$$M_{ijkl} = (\delta_{ik} - D_{ik})^{-1}\delta_{jl} \tag{20}$$

When the second order damage tensor becomes a scalar ($D_{11} = D_{22} = D_{33} = D$ and all other $D_{ij} = 0$), the damage effect tensor given in Eq. (20) reduces to the scalar form in Eq. (18). From Eq. (20), it is evident that the effective stress may be unsymmetric. Voyiadjis and Kattan (1999) have discussed three methods of symmetrization of M_{ijkl}, given by the forms:

$$\begin{aligned} \tilde{\sigma}_{ij} &= \frac{\sigma_{ik}(\delta_{kj} - D_{kj})^{-1} + (\delta_{il} - D_{il})^{-1}\sigma_{lj}}{2} && \text{(a)} \\ \tilde{\sigma}_{ij} &= (\delta_{ik} - D_{ik})^{-1/2}\sigma_{kl}(\delta_{lj} - D_{lj})^{-1/2} && \text{(b)} \\ \sigma_{ij} &= \frac{\tilde{\sigma}_{ik}(\delta_{kj} - D_{kj})^{-1} + (\delta_{il} - D_{il})^{-1}\tilde{\sigma}_{lj}}{2} && \text{(c)} \end{aligned} \tag{21}$$

The symmetrization forms of Eq. (21)(a) and (b) are popular in the literature and have been used in Chow and Wang (1987) and Zhu and Cescotto (1995). In Voyiadjis and Kattan (1999), various forms of M_{ijkl} are expressed in the principal

damage coordinate system of in terms of the principal values D_1, D_2, D_3. The sum type symmetrization based on Eq. (21)(a) leads to

$$M = \mathrm{diag}\left[\frac{1}{1-D_1}, \frac{1}{1-D_2}, \frac{1}{1-D_3}, \frac{(1-D_3)+(1-D_2)}{2(1-D_3)(1-D_2)}, \frac{(1-D_3)+(1-D_1)}{2(1-D_3)(1-D_1)}, \frac{(1-D_2)+(1-D_1)}{2(1-D_2)(1-D_1)}\right] \tag{22}$$

while the product type of symmetrization based on Eq. (21)(b) leads to

$$M = \mathrm{diag}\left[\frac{1}{1-D_1}, \frac{1}{1-D_2}, \frac{1}{1-D_3}, \frac{1}{\sqrt{(1-D_3)(1-D_2)}}, \frac{1}{\sqrt{(1-D_3)(1-D_1)}}, \frac{1}{\sqrt{(1-D_2)(1-D_1)}}\right] \tag{23}$$

The resulting damaged stiffness for an initially orthotropic material is deduced to be also orthotropic from Eq. (17) (see Carol et al., 1994).

The orthotropic damage model, with the second order damage tensor, is now examined for its effectiveness in representing interfacial debonding based damage in composite microstructures. The square RVE is described in Fig. 3 is analyzed by VCFEM for various different cases of loading with different combinations of strain along different strain paths. For this RVE, the global axes x and y correspond to planes of material symmetry. For any damage inducing load path, that may preserve the initial material symmetry (orthotropy for the composite RVE), the resulting damaged stiffness will be orthotropic in the global coordinate system. Straining paths corresponding to normal strain loading, i.e. $\epsilon_{xx} = \epsilon_{yy} \neq 0$, $\epsilon_{xy} = 0$, is found to cause debonding while preserving the original material symmetry axes. Consequently, the stiffness measured in the global coordinate system is always orthotropic for this loading and the second order damage tensor should be capable of representing this orthotropic damage.

Next, the RVE loaded in shear $\epsilon_{xx} = \epsilon_{yy} = 0$, $\epsilon_{xy} \neq 0$, for which the configuration upon completion of debonding is shown in Fig. 4. Homogenization of the micromechanics results for the undamaged and final damaged configurations leads to

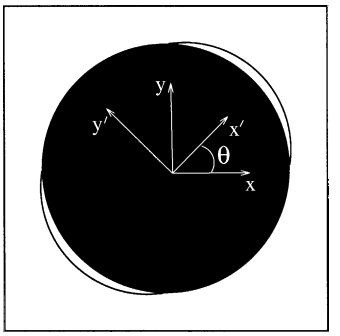

Fig. 4. Debonding pattern of a RVE subjected to shear loading.

Undamaged stiffness
(Global coordinates)

$$\begin{bmatrix} 12.39 & 7.60 & 0 & 7.55 \\ 7.60 & 12.39 & 0 & 7.55 \\ 0 & 0 & 2.16 & 0 \\ 7.55 & 7.55 & 0 & 51.39 \end{bmatrix}$$

$\Rightarrow$ Damaged stiffness
(Global coordinates)

$$\begin{bmatrix} 7.94 & 4.55 & -1.08 & 4.80 \\ 4.55 & 7.94 & -1.08 & 4.80 \\ -1.08 & -1.08 & 1.56 & -0.79 \\ 4.80 & 4.80 & -0.79 & 49.36 \end{bmatrix}$$

$\Rightarrow$ Damaged stiffness
(Rotated coordinates)

$$\begin{bmatrix} 5.65 & 4.69 & 0 & 4.01 \\ 4.69 & 9.97 & 0 & 5.59 \\ 0 & 0 & 1.70 & 0 \\ 4.01 & 5.59 & 0.0 & 49.36 \end{bmatrix}$$

This damaged stiffness exhibits coupling between the normal and shear strain components in the elastic energy evaluation, a feature that is not characteristic of orthotropy. Hence, the material exhibits general anisotropy in the global coordinate system. However, if the stiffness is transformed to the principal damage axes ($x' - y'$) by a rotation of $\theta = 45°$, the coupling vanishes and orthotropy of the stiffness matrix is regained. Thus the material is orthotropic with respect to the principal damage coordinate system. The debonding for this

case is see to be symmetric about the principal damage axes as shown in Fig. 4.

Finally a coupled tension/shear loading of the RVE, with $\epsilon_{xy}/\epsilon_{xx} = 2$ and $\epsilon_{yy} = 0$, is considered. The homogenized undamaged stiffness and stiffness at the final damaged configuration in the global co-ordinate system are derived as

Undamaged stiffness
(Global coordinates)in GPa

$$\begin{bmatrix} 12.39 & 7.60 & 0 & 7.55 \\ 7.60 & 12.39 & 0 & 7.55 \\ 0 & 0 & 2.16 & 0 \\ 7.55 & 7.55 & 0 & 51.39 \end{bmatrix}$$

$\Rightarrow$ Damaged stiffness
(Global coordinates)in GPa

$$\begin{bmatrix} 5.11 & 3.11 & -0.59 & 3.24 \\ 3.11 & 5.91 & -0.82 & 3.53 \\ -0.59 & -0.82 & 1.38 & -0.52 \\ 3.24 & 3.53 & -0.52 & 48.33 \end{bmatrix}$$

The coupling between the normal and shear components is once again observed for the damaged stiffness in the global coordinate system. In an attempt to determine the orientation of the local coordinate axes for which all the coupling terms vanish and hence the stiffness matrix orthotropic, a coordinate transformation is performed. The transformation rotated stiffness matrix at any angle θ measured from the global co-ordinate system can be written as

$$E^{\theta}_{ijkl} = T_{ip}T_{jq}T_{kr}T_{ls}E^{\theta=0^\circ}_{pqrs} \tag{24}$$

where T_{ij} is the rotation matrix with components

$$T_{ij} = \begin{bmatrix} \cos\theta & \sin\theta & 0 \\ -\sin\theta & \cos\theta & 0 \\ 0 & 0 & 1 \end{bmatrix}$$

Variations of the homogenized normal/shear coupling terms E_{1112}, E_{2212} and E_{3312} as functions of θ are plotted in Fig. 5. While the values of these three coefficients are close to zero near $\theta = 45^\circ$ and $\theta = 135^\circ$, they do not vanish simultaneously for any single value of θ. Consequently, it may be concluded that this material is not truly orthotropic in any coordinate system orientation and the undamaged material symmetries diminish with evolving damage.

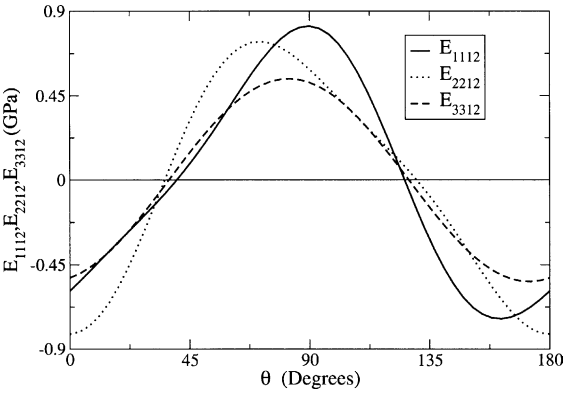

Fig. 5. Variation of stiffness matrix entries E_{1112}, E_{2212} and E_{3312} as a function of θ.

From the previous discussion, it is clear the even for the unit cell with a circular fiber, anisotropy sets in for the combined normal/shear coupled loading conditions. A specific case of $\frac{\epsilon_{xy}}{\epsilon_{xx}} = 2$ was discussed in detail. It is of interest to identify the error introduced in estimating the modulus, if orthotropy is assumed, for these combined normal-shear coupled loading conditions. To this end, analysis is performed with a strain ratio $\theta = \tan^{-1}(\frac{\epsilon_{xx}}{\epsilon_{xy}})$, for θ varying from 0° to 90°. The analysis is performed for all three cases considered (discussed in detail in Section 6), viz.: (a) unit cell with a circular fiber, (b) unit cell with an elliptical fiber and (c) a random distribution of 20 fibers. Fig. 6 shows the ratio of the normal–shear coupling stiffness term to the normal stiffness term $\frac{E_{1112}}{E_{1111}}$ for varying θ. It can be seen that the ratio can be as high as 16% measured in the global co-ordinate system. As θ approaches 90° corresponding to the case of pure tension loading, the ratio approaches 0. For the circular and elliptical fiber cases, this tension loading is symmetric with respect to both axes and thus does not induce any coupling terms in the global coordinate system. However, for the random case, there is no symmetry with respect to the global co-ordinate system and thus coupling term exists even for the case of pure tension loading.

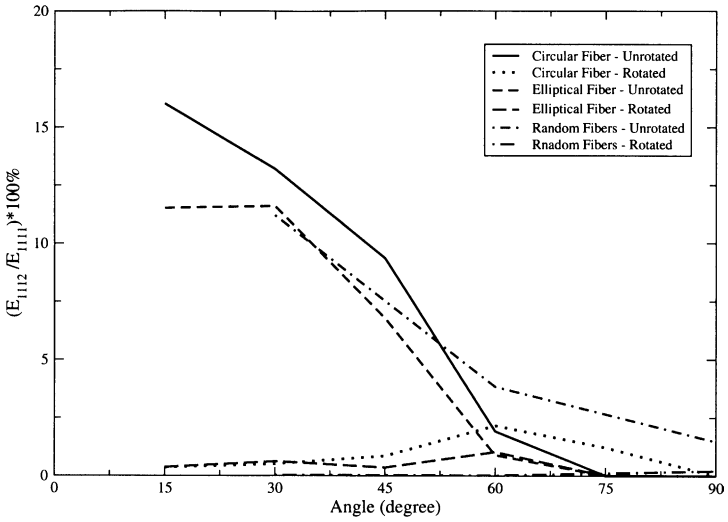

Fig. 6. Ratio of normal/shear coupling stiffness term E_{1112} to the normal term E_{1111} as a function of θ in both global and rotated co-ordinate system that makes E_{3312} zero.

The principal damage axis of these multi-axial loading is not known a-priori. To measure the extent of anisotropy, an axis is determined that makes one of the normal shear coupling term to go to zero. In this axis system, the other non-zero normal shear coupling terms are determined. To this end, the rotated E'_{3312} in terms of unrotated stiffness coefficients is given by using Eq. (24). The rotation angle θ is determined that makes E_{3312} zero. At this angle, the non-zero values of E'_{1112} and E'_{1111} are also calculated. The ratio of $\frac{E'_{1112}}{E'_{1111}}$ is provided in Fig. 6 as a measure of the extent of anisotropy. It can be seen that material is anisotropic in all co-ordinate system for these normal/shear combined loading. However, the degree of anisotropy is not as severe as in the global co-ordinate system and is around 2%. The figure also shows the relative values for the elliptical fiber and the random fiber cases. A similar behavior is observed with the ratio between the shear/normal stiffness at 10% or more in the global co-ordinate system and is less than 2% in the axis that makes one of the normal-shear term vanish.

It is interesting to mention that a Vakulenko–Kachanov type of second order tensor damage representation has been used by Talreja (1990) to predict change in the initial orthotropic symmetry for the general damage case and for debonding in Talreja (1991). Though an orthotropic damaged stiffness have been assumed by Lene and Leguillon (1982) in their asymptotic homogenization model for RVE's with interfacial debonding, their analysis is due to tangential slip only and any normal separation has been ignored. From the above study, it can be concluded that second order damage models are generally pretty good. However, in the intent of seeking an accurate representation of the damage behavior, an anisotropic damage model with a fourth order damage tensor is deemed suitable for macroscopic damage representation in this class of composites.

4.3. Anisotropic damage model with fourth order damage tensor

Anisotropic damage models involving forth order damage variables are able to overcome shortcomings of the other models discussed in the previous sections. Such models have been proposed by e.g. Ortiz (1985) for concrete in which loading surface is defined in stress space and the secant compliance tensor is considered as an internal variable. Simo and Ju (1987) have proposed a loading surface in the strain space with the current damaged stiffness tensor as an internal variable. Anisotropic damage in this work is introduced

through positive projection strain tensors. The proposed model in this paper extends the Simo–Ju strain based damage model to account the anisotropic evolution of stiffness degradation. The damage surface in this model is expressed in terms of the strain ϵ_{ij} and the damage work W_d as

$$F = \tfrac{1}{2}\epsilon_{ij}P_{ijkl}\epsilon_{kl} - \kappa(\alpha W_d) = 0 \tag{25}$$

where P_{ijkl} symmetric negative definite fourth order tensor that should be determined, α is a scaling parameter, κ is a parameter that is a function of the damage work $W_d = \int \frac{1}{2}\epsilon_{ij}\,\mathrm{d}E_{ijkl}\epsilon_{kl}$. It is important to introduce the scaling parameter in conjunction with the damage work to account for its variability with the loading path, as explained in Appendix A. From the definition of the rate of damage work $\dot{W}_d$, $\frac{1}{2}\epsilon_{ij}\epsilon_{kl}$ is the conjugate to $\dot{E}_{ijkl}$. Using the associativity rule, the rate of stiffness degradation can be obtained as

$$\dot{E}_{ijkl} = \dot{\lambda}\frac{\partial F}{\partial\left(\frac{1}{2}\epsilon_{ij}\epsilon_{kl}\right)} = \dot{\lambda}P_{ijkl} \tag{26}$$

It may be inferred from this Eq. (26) that P_{ijkl} corresponds to the direction of the rate of stiffness degradation tensor $\dot{E}_{ijkl}$. The model necessitates the evaluation of $\kappa(W_d)$, α and P_{ijkl}, which can be accomplished by micromechanical RVE analyses with periodicity boundary conditions. Determination of these parameters is discussed next.

4.4. Determination of $\kappa(W_d)$ and $\alpha(\epsilon_{ij})$

Evaluation of the function $\kappa(W_d)$ involves calculating this function for a reference loading path (strain combination) and scaling it for all other load paths with respect to this reference. In this paper, the reference loading path is chosen to be ($\epsilon_{xx} \neq 0$, all other $\epsilon_{ij} = 0$). Micromechanical simulation of the RVE is performed for this load path with periodic boundary conditions. The corresponding damage surface Eq. (25) for this loading becomes

$$\tfrac{1}{2}\epsilon_{xx}^2 P_{1111} - \kappa = 0 \tag{27}$$

Without loss of generality, the value of P_{1111} may be set to 1 and thus $\kappa = \frac{1}{2}\epsilon_{xx}^2$. The values of W_d can be evaluated numerically at the end of each increment. The functional form of $\kappa(W_d)$ is shown in Fig. 8. In the undamaged range, κ increases slightly for no damage work W_d. On the other hand, it asymptotically reaches an infinite value at the damage saturation value corresponding to W_d^F, since κ keeps increasing even without any increase in W_d. Once the maximum value W_d^F is determined for the reference loading condition, α for any strain path can be obtained by simple scaling as

$$\alpha(\epsilon_{xx}, \epsilon_{yy}, \epsilon_{xy}) = \frac{W_d(\epsilon_{xx}, \epsilon_{yy}, \epsilon_{xy})}{W_d(\epsilon_{xx} \neq 0, \epsilon_{yy} = 0, \epsilon_{xy} = 0)} \tag{28}$$

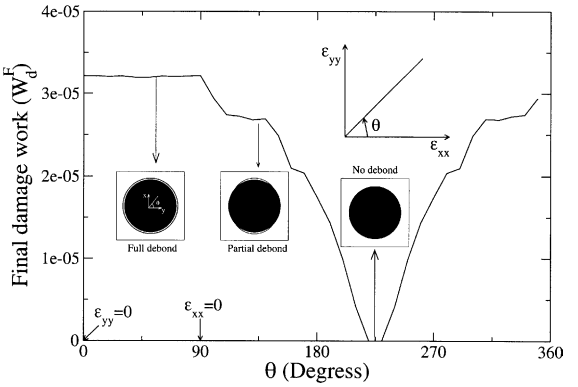

Fig. 7. Plot of final damage work vs angle θ for a RVE loaded along biaxial strain path.

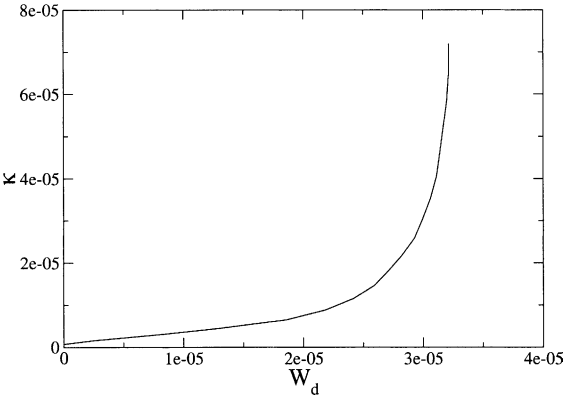

Fig. 8. Plot of κ vs. W_d for a RVE loaded along the macroscopic strain path $\epsilon_{xx} \neq 0$, $\epsilon_{yy} = \epsilon_{xy} = 0$.

4.5. Determination of $P_{ijkl}(\epsilon)$

The damage parameters P_{ijkl} have been assumed to be constant in the Neilsen and Schreyer

model described in Carol et al. (1994). However, for composite material with interfacial debonding, the direction of rate of stiffness degradation varies significantly with increasing damage. Fig. 9b show the progressive contour plots of σ_{xx} in a RVE undergoing interfacial debonding with increased straining, in a constrained tension test with $\epsilon_{xx} \neq 0, \epsilon_{yy} = \epsilon_{xy} = 0$ (Fig. 9a). The corresponding stiffness degradations are plotted as functions of the strain for two components E_{1111} and E_{2222} in Fig. 9c. At the initial stages of debonding, E_{1111} decreases faster than E_{2222} due to the location of initiation and direction of propagation of the debonding crack. It also stabilizes at a smaller strain in comparison with E_{2222}. At the final strain, when both stiffness components have stabilized at very low values, the RVE behavior is similar to that of a voided matrix with large porosity. The varying rates of stiffness degradation with increasing strain conclusively points to the fact that constant P_{ijkl} cannot capture this behavior. The components of $P_{ijkl}(\epsilon_{mn})$ are considered to be functions

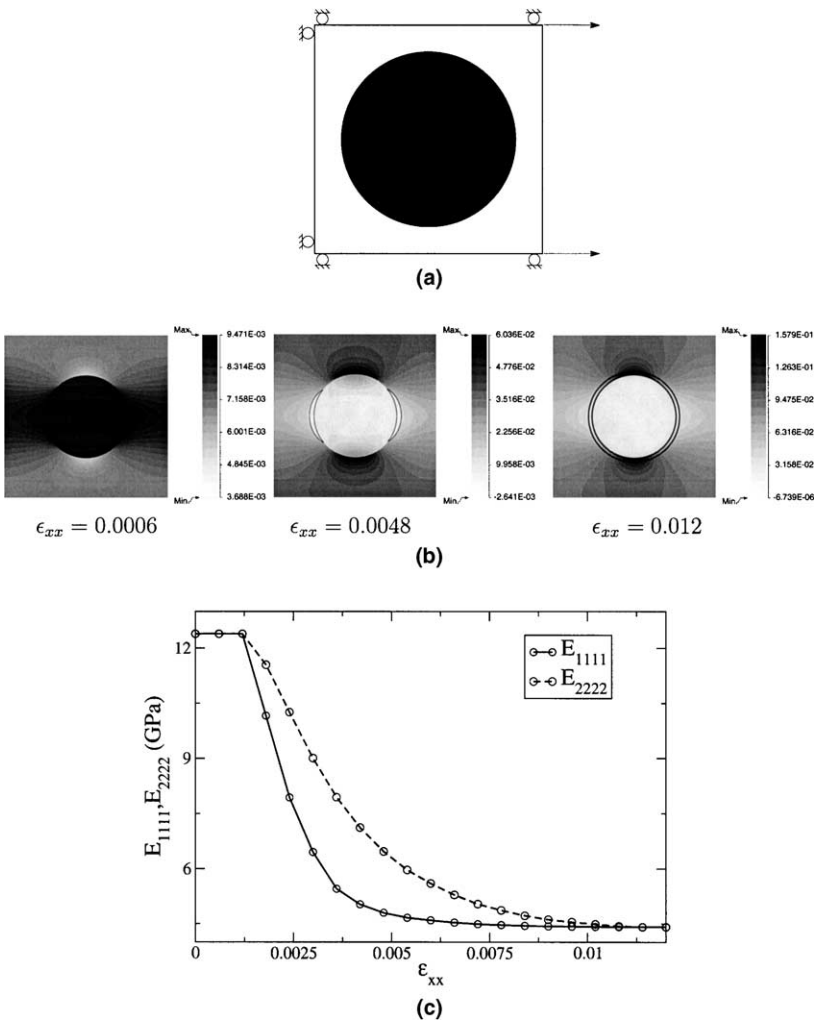

Fig. 9. (a) RVE subjected to loading conditions with $\epsilon_{xx} \neq 0$, $\epsilon_{yy} = 0$, $\epsilon_{xy} = 0$. (b) Plot of microscopic σ_{xx} contours with debonding for increasing loads. (c) Plot of degrading stiffness values E_{1111}, E_{2222} with increasing loads.

of the total strain and damage work, but their dependence on load history is assumed to be negligible in this work.

Due to the lack of a comprehensive functional form of $P_{ijkl}(\epsilon_{mn})$, a discrete approach, similar to that used in FEM is adopted in this paper. Discrete values of P_{ijkl} are evaluated at points in the macroscopic strain space by homogenization of the RVE-micromechanics analyses at systematic intervals along various strain paths. In the discretized strain space of Fig. 10, the value of a piecewise continuous P_{ijkl} at any point in the strain space may then be obtained by interpolation from nodal values according to

$$P_{ijkl}(\epsilon_{xx},\epsilon_{yy},\epsilon_{xy}) = \sum_{\alpha=1}^{8} (P_{ijkl})_\alpha N_\alpha(\epsilon_{xx},\epsilon_{yy},\epsilon_{xy}) \tag{29}$$

where $(P_{ijkl})_\alpha$ are the nodal values and N_α are the shape functions for a 3D linear 8-noded hexahedral element. A similar process has been discussed for porous elasto-plasticity in Lee and Ghosh (1999).

The nodal values of macroscopic stresses, the corresponding damage work W_d and P_{ijkl} are evaluated at each nodal point in a subspace of the ϵ_{xx}–ϵ_{yy}–ϵ_{xy} space by solving incremental microscopic boundary value problems with VCFEM and asymptotic homogenization. In this process, macroscopic strain increments are applied to the RVE subjected to periodic boundary conditions (see Lee and Ghosh, 1999). Strain increments are applied along the radial line in the macroscopic strain space such that a constant ratio is maintained between the strain components, i.e. $\Delta\epsilon_{xx}:\Delta\epsilon_{yy}:\Delta\epsilon_{xy} = \cos\theta\cos\phi:\sin\theta\cos\phi:\sin\phi$, where the angles θ and ϕ are depicted in Fig. 10. From the symmetry conditions, only half of the ϵ_{xx}–ϵ_{yy}–ϵ_{xy} strain space is considered for loading, such that $0° \leqslant \theta \leqslant 360°$ in the ϵ_{xx}–ϵ_{yy} plane and $0° \leqslant \phi \leqslant 90°$ outside of this plane. The microscopic shear behavior is identical about the ϵ_{xx}–ϵ_{yy} plane except for the sign and hence only the positive part is retained in ϕ range. The θ range encompasses the entire ϵ_{xx}–ϵ_{yy} plane, since the microscopic debonding behavior in tension and compression are different. The analyses are performed at uniform strain intervals of $\Delta\theta = 10°$, $\Delta\phi = 15°$. The evaluation procedure is detailed below.

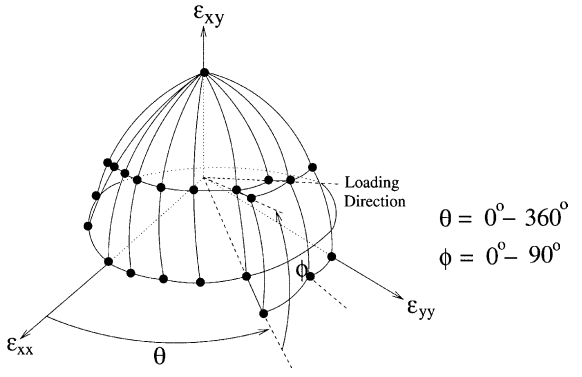

Fig. 10. Discretised macroscopic strain space for P_{ijkl} evaluation where the strain increments are prescribed as $\Delta\epsilon_{xx}:\Delta\epsilon_{yy}:\Delta\epsilon_{xy} = \cos\theta\cos\phi:\sin\theta\cos\phi:\sin\phi$.

For a strain increment from step n to step $n+1$, the evolution equation (26) may be integrated by trapezoidal rule to give

$$(E_{ijkl})_{n+1} - (E_{ijkl})_n = \tfrac{1}{2}(\lambda_{n+1} - \lambda_n)((P_{ijkl})_{n+1} + (P_{ijkl})_n) \tag{30}$$

Assuming that all quantities at step n are known, $(P_{ijkl})_{n+1}$ can be evaluated from

$$(P_{ijkl})_{n+1} = \frac{2((E_{ijkl})_{n+1} - (E_{ijkl})_n)}{\lambda_{n+1} - \lambda_n} - (P_{ijkl})_n \tag{31}$$

$(E_{ijkl})_{n+1}$ is the secant stiffness at the end of the increment, calculated by performing homogenization of micromechanical variables at the end of the increment followed by unloading to the origin. The remaining parameter λ_{n+1} is evaluated from the consistency condition. Eq. (25) yields

$$F_{n+1} = 0 \quad \Rightarrow \quad \tfrac{1}{2}(\epsilon_{ij})_{n+1}(P_{ijkl})_{n+1}(\epsilon_{kl})_{n+1} - \kappa_{n+1} = 0 \tag{32}$$

By substitution of Eq. (31), this becomes

$$\frac{1}{2}(\epsilon_{ij})_{n+1}\left(2\frac{(E_{ijkl})_{n+1} - (E_{ijkl})_n}{\lambda_{n+1} - \lambda_n} - (P_{ijkl})_n\right) \times (\epsilon_{kl})_{n+1} - \kappa_{n+1} = 0 \tag{33}$$

where $\kappa_{n+1}(\alpha W_{dn+1})$ represents the size of the parametric damage surface. $\alpha(\epsilon_{ij})$ is evaluated from Eq. (28) using the procedure outlined in Section 4.4 and W_d is evaluated for the current increment using Eq. (A.1). λ_{n+1} is then evaluated from

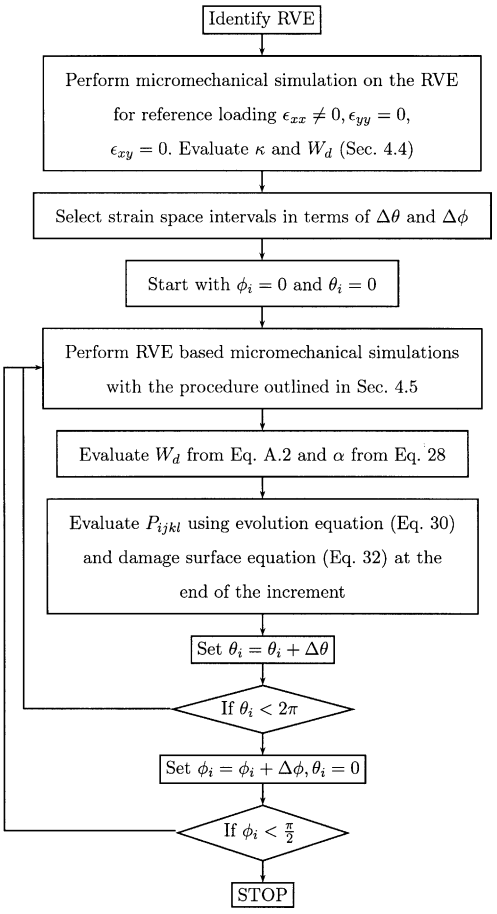

Fig. 11. Flow chart for damage parameter evaluation.

$$\lambda_{n+1} = \lambda_n + \frac{\frac{1}{2}(\epsilon_{ij})_{n+1} 2((E_{ijkl})_{n+1} - (E_{ijkl})_n)(\epsilon_{kl})_{n+1}}{\kappa_{n+1} + \frac{1}{2}(\epsilon_{ij})_{n+1}(P_{ijkl})_n(\epsilon_{kl})_{n+1}} \tag{34}$$

Finally $(P_{ijkl})_{n+1}$ is determined from Eq. (31) and stored in a numerical database. A flow chart of the parameter evaluation process for the anisotropic damage model is provided in Fig. 11.

5. Stress update algorithm for macroscopic analysis

The anisotropic continuum damage model, developed from rigorous RVE-based micromechanical analysis as discussed in Section 4.3, is implemented in an incremental small-deformation macroscopic finite element analysis model. An important ingredient of this macroscopic model is the integration algorithm for obtaining stresses $(\sigma_{ij})_{n+1}$ at the current strain value $(\epsilon_{ij})_{n+1}$, assuming that all necessary variables are known at step n. The essential steps in this process are itemized below.

- For the prescribed current strain value $(\epsilon_{ij})_{n+1}$, evaluate $(P_{ijkl})_{n+1}$ by interpolation in the discretized strain space of Fig. 10 using Eq. (29). Similarly determine $\alpha(\epsilon) = \sum_{\beta=1}^{4} \alpha_\beta N_\beta (\epsilon_{xx}, \epsilon_{yy}, \epsilon_{xy})$.
- If $\frac{1}{2}(\epsilon_{ij})_{n+1}(P_{ijkl})_{n+1}(\epsilon_{kl})_{n+1} - \kappa_n(\alpha(W_d)_n) \leqslant 0 \Rightarrow$ loading without damage In this case, the stresses are updated as

$$(\sigma_{ij})_{n+1} = (E_{ijkl})_n(\epsilon_{kl})_{n+1} \tag{35}$$

- Damage evolution takes place when

$$\frac{1}{2}(\epsilon_{ij})_{n+1}(P_{ijkl})_{n+1}(\epsilon_{kl})_{n+1} - \kappa_n(\alpha(W_d)_n) > 0 \tag{36}$$

  For this case, (a) determine $\kappa_{n+1} = \frac{1}{2}(\epsilon_{ij})_{n+1}(P_{ijkl})_{n+1}(\epsilon_{kl})_{n+1}$ from the consistency condition.(b) Determine W_d from κ–W_d plot.
- From the definition of W_d and using Eq. (26)

$$\dot{W}_d = \frac{1}{2}\epsilon_{ij}\dot{E}_{ijkl}\epsilon_{kl} = \tfrac{1}{2}\dot{\lambda}\epsilon_{ij}P_{ijkl}\epsilon_{kl} \tag{37}$$

  Integrating Eq. (37) with trapezoidal rule

$$(W_d)_{n+1} - (W_d)_n = \frac{1}{2}\left[\frac{1}{2}(\lambda_{n+1} - \lambda_n)((\epsilon_{ij}P_{ijkl}\epsilon_{kl})_{n+1} + (\epsilon_{ij}P_{ijkl}\epsilon_{kl})_n)\right] \tag{38}$$

  from which λ_{n+1} is determined as

$$\lambda_{n+1} = \lambda_n + \frac{4((W_d)_{n+1} - (W_d)_n)}{((\epsilon_{ij}P_{ijkl}\epsilon_{kl})_{n+1} + (\epsilon_{ij}P_{ijkl}\epsilon_{kl})_n)} \tag{39}$$

- Finally, the secant stiffness and stresses are updated as

$$(E_{ijkl})_{n+1} = (E_{ijkl})_n + \frac{1}{2}(\lambda_{n+1} - \lambda_n)((P_{ijkl})_n + (P_{ijkl})_{n+1})$$
$$(\sigma_{ij})_{n+1} = (E_{ijkl})_{n+1}(\epsilon_{kl})_{n+1} \tag{40}$$

6. Numerical examples with the anisotropic damage model

The macroscopic finite element model with its constitutive relations represented by the continuum damage mechanics (CDM) model is validated by comparison of results with those obtained by homogenizing VCFEM solutions in the RVE. The macroscopic model consists of a single QUAD4 element. For the microstructure, three different RVE's are considered. These are represented by:

(a) a square domain with a circular fiber of volume fraction 20% (see Fig. 12a),

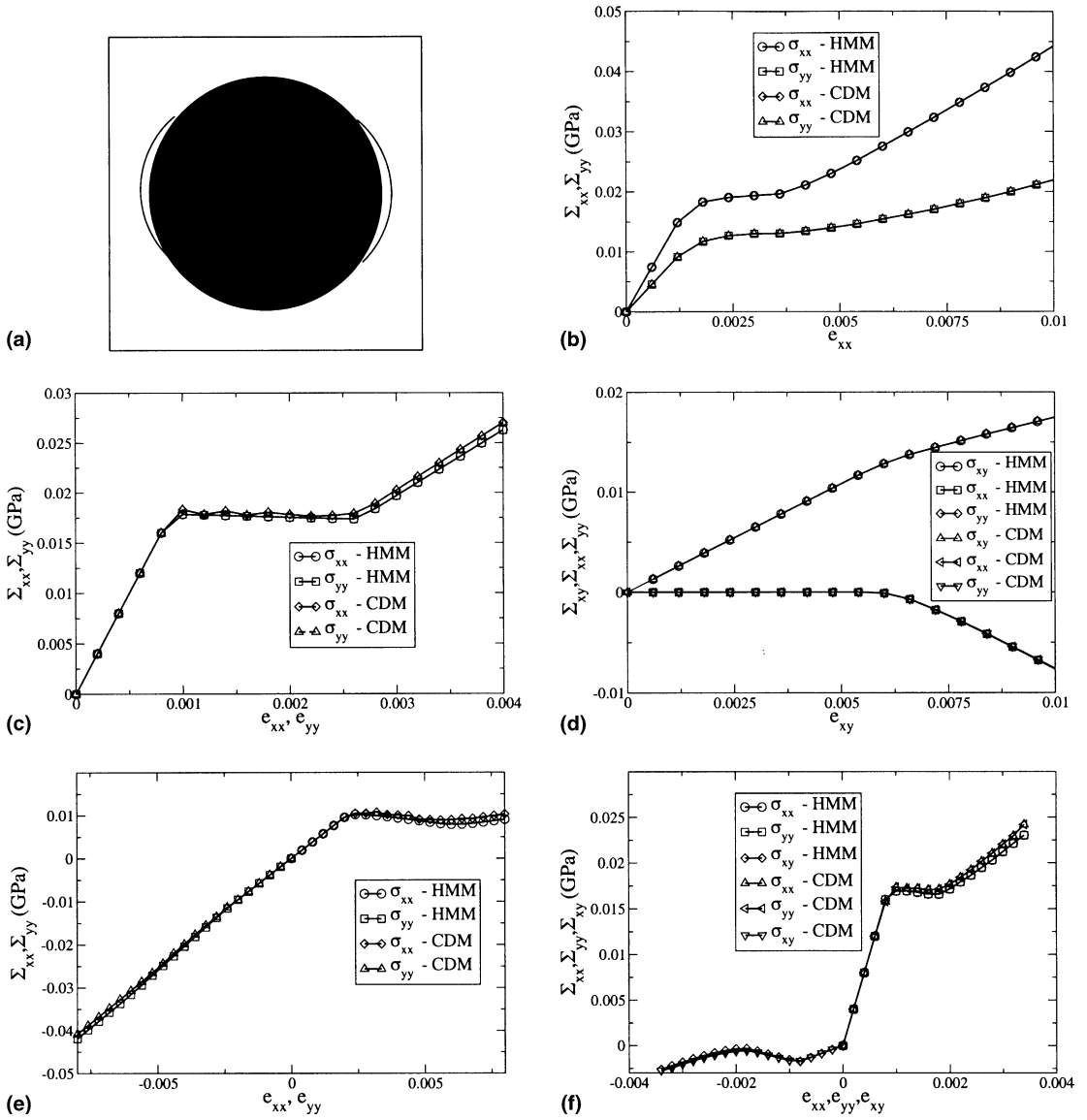

Fig. 12. Comparison of macroscopic stress–strain curves by Continuum Damage Model and Homogenized Micromechanics for a (a) RVE with circular fiber for load cases (b) L1, (c) L2, (d) L3, (e) L4 and (f) L5.

(b) a square domain with elliptical fiber of volume fraction 18.16% and aspect ratio $\frac{a}{b} = 2$ (see Fig. 13a), and

(c) a non-uniform RVE with 20 circular fibers of volume fraction 21.78% (see Fig. 14a). The construction of a non-uniform RVE with periodic boundary procedure has been explained in details in Raghavan and Ghosh (2004) and Raghavan and Ghosh (2004). Briefly speaking, a local extended microstructure is first constructed by repeating the set of randomly distributed fibers that lie in a window in both the y_1 and y_2 directions for several period lengths. For each fiber at (x, y), periodically

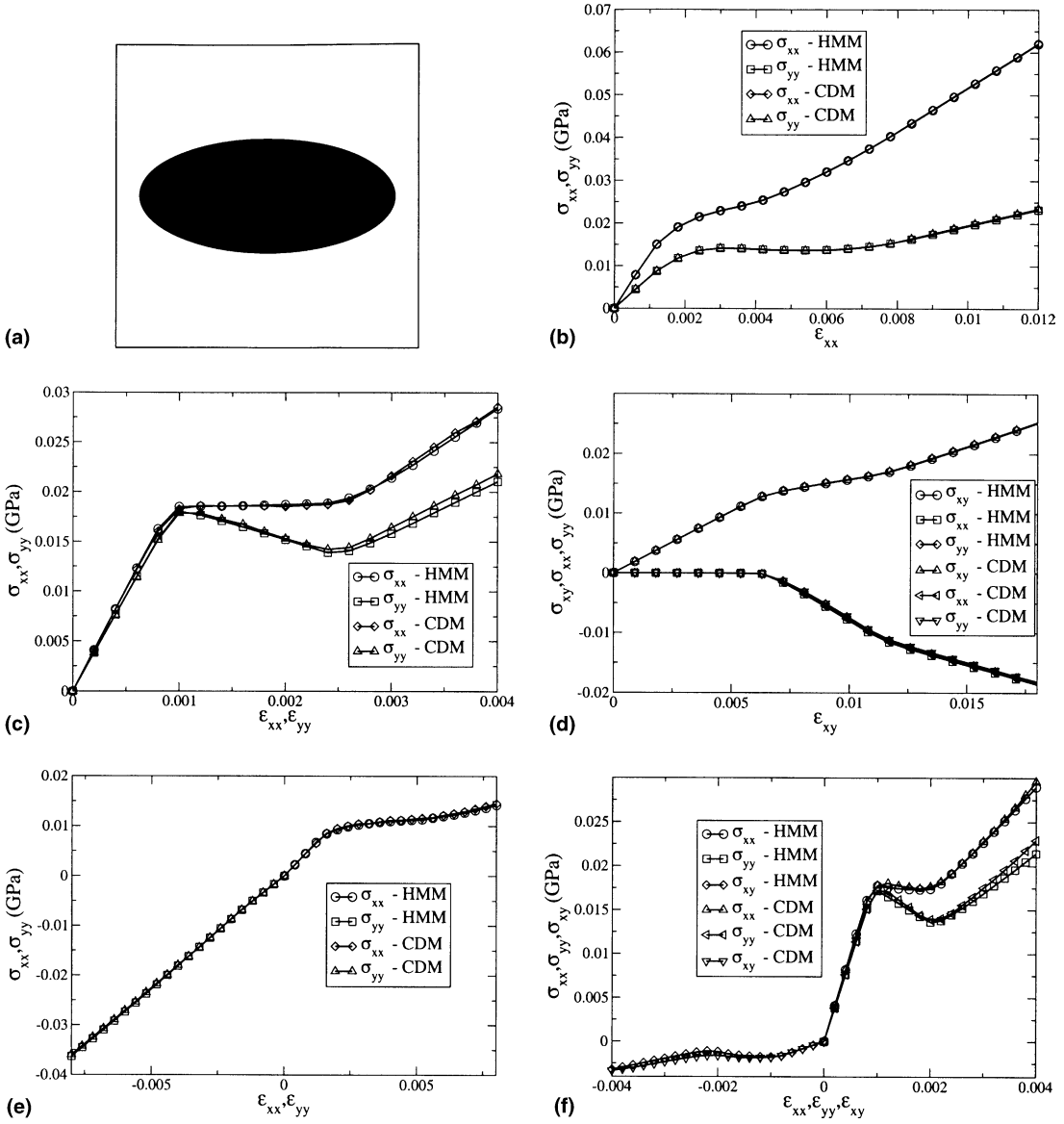

Fig. 13. Comparison of macroscopic stress–strain curves by Continuum Damage Model and Homogenized Micromechanics for a (a) RVE with elliptical fiber for load cases, (b) L1 (c) L2 (d) L3 (e) L4 (f) L5.

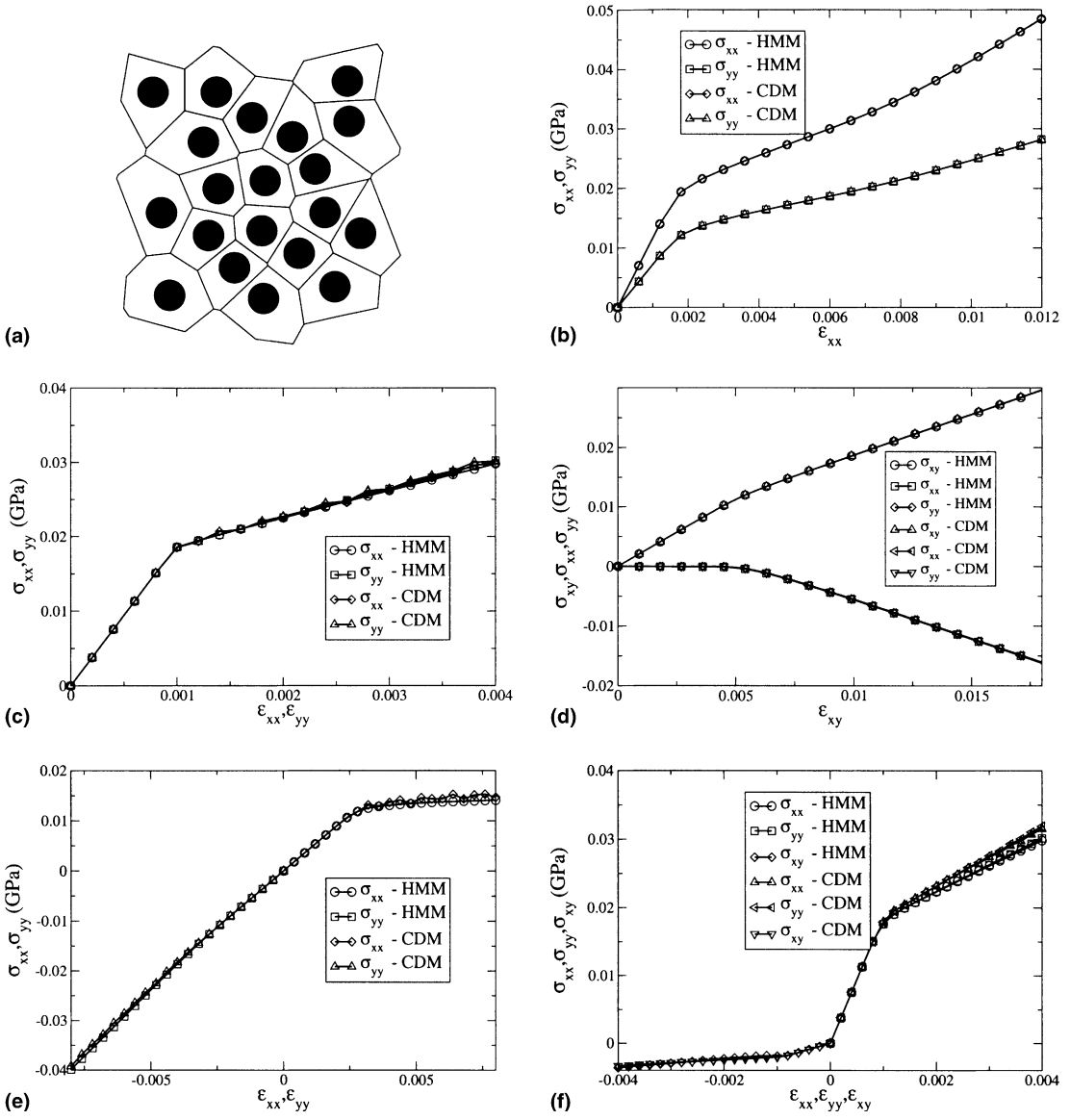

Fig. 14. Comparison of macroscopic stress–strain curves by Continuum Damage Model and Homogenized Micromechanics for a (a) random RVE with 20 circular fiber for load cases, (b) L1, (c) L2, (d) L3, (e) L4 and (f) L5.

repetitive fibers are placed at $(x \pm k_1 X, y)$, $(x, y \pm k_2 Y)$ and $(x \pm k_1 X, y \pm k_2 Y)$, where k_1, k_2 are integers and X, Y are the periods in the two directions. The multi-fiber domain is then tessellated into a network of Voronoi cells for the entire region and the boundary of the RVE is generated as the aggregate of the outside edges of Voronoi cells associated with the original set of fibers. The resulting SERVE will have non-straight line edges corresponding to non-uniform fiber arrangements. However, nodes on the RVE boundary, created by this procedure are periodic, i.e. for every boundary node a periodic pair can be identified on the boundary at a distance of one period along one or both of the coordinate directions.

Periodicity constraint conditions on nodal displacements can then be easily imposed by constraining the node pairs to move identically.

The material properties of the elastic matrix are $E_m = 4.6$ GPa, $\nu_m = 0.4$ and the elastic fiber are $E_f = 210$ GPa, $\nu_f = 0.3$. The interface properties are $\delta_c = 5.0 \times 10^{-5}$, $\delta_e = 20 \times 10^{-4}$ and $\sigma_m = 0.02$ GPa. Five different macroscopic strain paths are considered for loading conditions, viz.

$$\text{L1} : \epsilon_{xx} \neq 0, \epsilon_{yy} = \epsilon_{xy} = 0 \qquad \text{(Reference Loading)}$$

$$\text{L2} : \epsilon_{xx} = \epsilon_{yy} \neq 0, \epsilon_{xy} = 0$$

$$\text{L3} : \epsilon_{xy} \neq 0, \epsilon_{xx} = \epsilon_{yy} = 0$$

$$\text{L4} : \epsilon_{xx} = -\epsilon_{yy} \neq 0, \epsilon_{xy} = 0$$

$$\text{L5} : \epsilon_{xx} = \epsilon_{yy} = -\epsilon_{xy} \neq 0$$

Periodicity conditions are enforced on the boundaries. The parameter $\kappa(W_d)$ is evaluated from the reference loading (L1) corresponding to uniaxial tension. The strain states (L2) and (L3) correspond to biaxial and shear loading conditions respectively, while a combined tension–compression condition is represented by the load (L4). Finally the load (L5) represents a combination of all strain components.

The macroscopic stress–strain plots with the CDM model are compared with the homogenized micromechanical analyses in Fig. 12b–f. All the non-zero stress components are plotted for each of the five loading conditions and excellent agreement is observed. For the biaxial loading, the interface fails completely at a strain of 0.0025. After this, the material exhibits a constant stiffness corresponding to a RVE with a void. In the shear loaded case, while σ_{xx} and σ_{yy} are zero prior to the onset of damage, they continue to increase with softening and debonding of the interface. This is due the different interface behavior in tension and compression. For the tension–compression case (L4), the behavior is almost linear in compression, whereas the macroscopic stresses in tension are significantly lower due to damage. For the combined straining case, a more complex stress–strain behavior is observed.

For the RVE(b)containing an elliptical fiber, the comparisons are depicted in Fig. 13b–f. Once again, excellent agreement is observed between the CDM and the micromechanical analyses. The anisotropy caused by the elliptical shape results in a significant difference in the composite behavior in different directions. This anisotropy exists in the undamaged configuration, but gets pronounced with evolving damage because of the sensitivity of the damage path to the interface shape. Finally, Fig. 14b–f again demonstrate excellent agreement between CDM and micromechanics solutions for the RVE (c) with non-uniform fiber distribution. In this case, the VCFEM mesh is generated by tessellation of the RVE microstructure. It is interesting to note that the sharp difference in stiffness between the damaging and fully damaged states as observed in the previous two RVE's is not seen in this case for biaxial loading. The debonding initiation and propagation in this cases is dispersed in the microstructure and hence a very gradual reduction of stiffness is observed. The response is also more isotropic than the other cases for this microstructure. In all cases, the CDM model developed in this work, predicts the true homogenized damage behavior with high accuracy.

7. Conclusions

A robust macroscopic Continuum Damage Mechanics (CDM) model is developed for unidirectional fiber reinforced composites with interfacial debonding, in this paper. The anisotropic CDM model using fourth order damage tensor, in which the stiffness is characterized as an internal variable, is found to perform most accurately for this class of materials. The development of the model involves micromechanical analysis of the RVE using the Voronoi cell FEM (VCFEM) with subsequent homogenization. Parameters in the CDM model, describing the anisotropic stiffness degradation, vary significantly with evolving damage and microstructural variables. A rigorous calibration framework for these parameters from micromechanical analysis is developed, such that their variations follow the real behavior during

composite failure. Specifically, a method for constructing damage-work dependent, piecewise continuous, anisotropic damage parameters is proposed by utilizing incremental loading paths and discrete data in the strain space. The methods make it possible to create a microstructure-based anisotropic damage surface in the strain space for which a continuous functional representation is difficult. Numerical examples are conducted with this CDM for RVE's with significantly different microstructures under a wide variety of loading paths, represented by various strain combinations. Simultaneously micromechanical analyses of the RVE-based problems are executed using VCFEM for subsequent homogenization. The comparison between CDM and homogenized micromechanics results show excellent agreement. Hence the CDM model is deemed suitable for implementing in macroscopic finite element codes to represent damage evolution in composites. It should be emphasized that the computational efficiency gained by this effective CDM model is significant when compared with the performance of two-scale damage models using asymptotic homogenization like (Fish et al., 1999; Lene and Leguillon, 1982).

However, the model proposed is restricted by the assumptions of the existence of a RVE in the presence of micro-damage. Effectively this means that it assumes uniformity of macroscopic variables as well as microscopic periodicity. Bulsara et al. (1999) have studied methods of RVE size determination for non-uniform distribution with damage. Lacy et al. (1999) have proposed higher order internal state variables based on the gradients of mesoscale damage distribution for RVE containing distributed micro-cracks. It is well known that catastrophic failure occurs by the localization of damage, resulting in sever gradients. The present model will not be applicable in these regions because of its local nature. These regions would need the models to transcend scales to capture the localized damage growth as suggested in the multi-scale model of Ghosh et al. (2001) and Raghavan and Ghosh (2004). A true multi-scale model with the CDM model developed in this paper is the subject of a future paper.

Acknowledgments

This work has been supported by the Air Force Office of Scientific Research through grant no. F49620-98-1-01-93 (Program Director: Dr. B.L. Lee). This sponsorship is gratefully acknowledged. Computer support by the Ohio Supercomputer Center through grant no. PAS813-2 is also gratefully acknowledged.

Appendix A. Scaling parameter for variability in damage work with load history

In continuum damage mechanics, the total damage work may be considered as an internal variable denoting the current state of damage. The total damage work W_d is expressed as (see Carol et al., 1994):

$$W_d = \int \frac{1}{2}\epsilon_{ij}\epsilon_{kl}\,\mathrm{d}E_{ijkl} \tag{A.1}$$

In an incremental numerical method used for determining the evolving damage process, a trapezoidal rule may be used to additively calculate the damage work over n strain increments, given as

$$\begin{aligned} W_d &= \int_{\epsilon_{ij}^0}^{\epsilon_{ij}^1} \frac{1}{2}\epsilon_{ij}\epsilon_{kl}\,\mathrm{d}E_{ijkl} + \int_{\epsilon_{ij}^1}^{\epsilon_{ij}^2} \frac{1}{2}\epsilon_{ij}\epsilon_{kl}\,\mathrm{d}E_{ijkl} \\ &\quad + \cdots + \int_{\epsilon_{ij}^{n-1}}^{\epsilon_{ij}^n} \frac{1}{2}\epsilon_{ij}\epsilon_{kl}\,\mathrm{d}E_{ijkl} \\ &= \frac{1}{2}\left[\frac{1}{2}(E_{ijkl}^1 - E_{ijkl}^0)(\epsilon_{ij}^1\epsilon_{ij}^1 + \epsilon_{ij}^0\epsilon_{ij}^0)\right. \\ &\quad + \frac{1}{2}(E_{ijkl}^2 - E_{ijkl}^1)(\epsilon_{ij}^2\epsilon_{ij}^2 + \epsilon_{ij}^1\epsilon_{ij}^1) \\ &\quad \left. + \cdots + \frac{1}{2}(E_{ijkl}^n - E_{ijkl}^{n-1})(\epsilon_{ij}^n\epsilon_{ij}^n + \epsilon_{ij}^{n-1}\epsilon_{ij}^{n-1})\right] \end{aligned} \tag{A.2}$$

The stiffness components E_{ijkl} at the end of each increment are computed by homogenization of the corresponding micromechanical variables. Prior to the onset of debonding, the damage work will be zero since $\dot{E}_{ijkl}$ is zero. As the interface debonds with separation increasing beyond δ_c, softening and subsequent debonding causes the

stiffness degradation rate $\dot{E}_{ijkl}$ to be non-zero, resulting in increase of damage work. The rate $\dot{E}_{ijkl}$ becomes zero once again, when the maximum interfacial debonding has occurred. The total damage work for any loading path reaches a maximum value at this arrested debonding position.

The total damage work at the final configuration, corresponding to arrested interfacial debonding, varies considerably with load path or applied strains. This variability is examined by analyzing the RVE in Section 4, subjected to different strain paths. Specifically various combinations of $\epsilon_{xx} \neq 0$ and $\epsilon_{yy} \neq 0$ with $\epsilon_{xy} = 0$ are considered in this study. For each case, the ratio $\frac{\epsilon_{yy}}{\epsilon_{xx}}$ is maintained at a constant for the entire load history till the final debonding state has been realized. In Fig. 7 the final total damage work (W_d^F) in the RVE is plotted as a function of the applied strain combination, represented by the angle $\theta = \tan^{-1}\frac{\epsilon_{yy}}{\epsilon_{xx}}$ for each applied strain combination. For each load path, the strains may be expressed by a vector in the two dimensional strain space with components ($\epsilon_{xx} = r\cos\theta$, $\epsilon_{yy} = r\sin\theta$) for increasing r, as shown in Fig. 7 (inset). In this diagram, the case $\theta = 0°$ corresponds to uniaxial tension in the x direction while $\theta = 225°$ corresponds to a state of pure biaxial compression. A systematic sequence on RVE-based micromechanical analysis is performed in 10° increments of θ, and the corresponding W_d^F is recorded. Significant variation in W_d^F is seen as a function of the strain path. All angles between $\theta = 0°$ and $\theta = 90°$ correspond to some amount tension in both directions, for which almost all points on the interface finally debonds. Hence the work W_d^F is relatively independent of θ in this range. For angles $\theta > 90°$, there is some amount of compression in either one or both directions, which leads to only a partial debonding of the interface in the final configuration. This results in a reduction of W_d^F. For $\theta = 225°$, all points on the interface are in pure compression and $W_d^F = 0$. It is interesting to note that the variation of W_d^F from $\theta = 90°$ and $\theta = 360°$ is symmetric about $\theta = 225°$. Altenbach et al. (2001) have also observed a similar load dependence of hardening in plastic behavior of grey cast iron and have introduced a stress-based correction factor.

References

Altenbach, H., Stoychev, G.B., Tushtev, K.N., 2001. On elastoplastic deformation of grey cast iron. Int. J. Plasticity 17, 719–736.

Benveniste, Y., 1983. On the Mori-Tanaka's method in cracked bodies. Mech. Res. Comm. 13, 193–201.

Budiansky, B., O'Connell, R.J., 1976. Elastic moduli of a cracked solid. Int. J. Solids Struct. 12, 81–97.

Bulsara, V.N., Talreja, R., Qu, J., 1999. Damage initiation under transverse loading of unidirectional composites with arbitrarily distributed fibers. Comput. Sci. Tech. 59, 673–682.

Camacho, G.T., Ortiz, M., 1996. Computational modeling of impact damage in brittle materials. Int. J. Solids Struct. 33 (20–22), 2899–2938.

Carol, I., Rizzi, E., Willam, K., 1994. A unified theory of elastic degradation and damage based on a loading surface. Int. J. Solids Struct. 31 (20), 2835–2865.

Chaboche, J.L., 1981. Continuum damage mechanics. A tool to describe phenomena before crack initiation. Nucl. Engrg. Design 64, 233–247.

Chandra, N., Li, H., Shet, C., Ghonem, H., 2002. Some issues in the application of cohesive zone models for metal–ceramic interfaces. Int. J. Solids Struct. 39 (10), 2827–2855.

Choi, J., Tamma, K.K., 2001a. Woven fabric composites—Part I: Prediction of homogenized elastic properties and micromechanical damage analysis. Int. J. Numer. Methods Engrg. 50, 2285–2298.

Choi, J., Tamma, K.K., 2001b. Woven fabric composites—Part II: Characterization of macro-crack initiation loads for global damage analysis. Int. J. Numer. Methods Engrg. 50, 2299–2315.

Chow, C.L., Wang, J., 1987. An anisotropic theory of elasticity for continuum damage mechanics. Int. J. Fract. 20, 381–390.

Cordebois, J.P., Sidoroff, F., 1982. Anisotropic damage in elasticity and plasticity. J. Mec. Theor. Appl., 45–60.

Feng, W.W., 1991. A failure criterion for composite materials. J. Comp. Mater. 25, 88–100.

Fish, J., Yu, Q., Shek, K., 1999. Computational damage mechanics for composite materials based on mathematical homogenization. Int. J. Numer. Methods Engrg. 45, 1657–1679.

Ghosh, S., Mukhopadhyay, S.N., 1991. A two dimensional automatic mesh generator for finite element analysis of randomly dispersed composites. Comput. Struct. 41, 245–256.

Ghosh, S., Lee, K., Moorthy, S., 1995. Multiple scale analysis of heterogeneous elastic structures using homogenization theory and Voronoi cell finite element method. Int. J. Solids Struct. 32 (1), 27–62.

Ghosh, S., Lee, K., Raghavan, P., 2001. A multi-level computational model for multi-scale damage analysis in composite and porous materials. Int. J. Solids Struct. 38 (14), 2335–2385.

Ghosh, S., Ling, Y., Majumdar, B., Kim, R., 2000. Interfacial debonding analysis in multiple fiber reinforced composites. Mech. Mater. 32, 561–591.

Geubelle, P.H., 1995. Finite deformation effects in homogeneous and interfacial fracture. Int. J. Solids Struct. 32, 1003–1016.

Hansen, N.R., Schreyer, H.L., 1994. A thermodynamically consistent framework for theories of elastoplasticity coupled with damage. Int. J. Solids Struct. 31 (3), 359–389.

Hashin, Z., 1980. Failure criteria for unidirectional fiber composites. J. Appl. Mech. 47, 329–334.

Kachanov, L.M., 1987. Introduction to Continuum Damage Mechanics. M. Nijhoff, Boston, Dordrecht.

Krajicinovic, D., 1996. Damage Mechanics. Elsevier, Amsterdam.

Krajicinovic, D., Fonseka, G.U., 1981. Damage mechanics. The continuous damage theory of brittle materials. J. Appl. Mech. 48, 809–824.

Lacy, T.E., McDowell, D.L., Talreja, R., 1999. Gradient concepts for evolution of damage. Mech. Mater. 31, 831–860.

Lee, K., Ghosh, S., 1999. A microstructure based numerical method for constitutive modeling of composite and porous materials. Mater. Sci. Engng. A272, 120–133.

Lemaitre, J., Chaboche, J.L., 1990. Mechanics of Solids. Cambridge University Press.

Lene, F., Leguillon, D., 1982. Homogenized constitutive law for a partially cohesive composite material. Int. J. Solids Struct. 18 (5), 443–458.

Li, S., Ghosh, S., under review. Influence of the local morphology to interfaces in multiple fiber reinforced composites.

Lissenden, C.J., Herakovich, C.T., 1995. Numerical modeling of damage development and viscoplasticity in metal matrix composites. Comput. Methods Appl. Mech. Engrg. 126, 289–303.

Moorthy, S., Ghosh, S., 1996. A model for analysis of arbitrary composite and porous microstructures with Voronoi cell finite elements. Int. J. Numer. Methods Engrg. 39, 2363–2398.

Moorthy, S., Ghosh, S., 2000. Adaptivity and convergence in the Voronoi cell finite element model for analyzing heterogeneous materials. Comput. Methods Appl. Mech. Engrg. 185, 37–74.

Needleman, A., 1992. Micromechanical modeling of interfacial decohesion. Ultramicroscopy 40, 203–214.

Needleman, A., 1990. An analysis of tensile decohesion along an interface. J. Mech. Phys. Solids 38, 289–324.

Nemat-Nasser, S., Hori, M., 1999. Micromechanics: Overall Properties of Heterogeneous Materials. North-Holland, Elsevier, Amsterdam.

Horii, M., Nemat-Nasser, S., 1987. Interacting micro-cracks near the tip in process zone of a macro-crack. J. Mech. Phys. Solids 35, 601–629.

Ortiz, M., 1985. A constitutive theory for the inelastic behavior of concrete. Mech. Mater. 4, 67–93.

Ortiz, M., Pandolfi, A., 1999. Finite-deformation irreversible cohesive element for three-dimensional crack-propagation analysis. Int. J. Numer. Methods Engrg. 44, 1267–1282.

Park, T., Voyiadjis, G.Z., 1997. Damage analysis and elasto-plastic behavior of metal matrix composites using the finite element method. Engrg. Fract. Mech. 56 (5), 623–646.

Pyrz, R., 1994a. Quantitative description of the microstructure of Composites, Part 1: Morphology of unidirectional composite systems. Comput. Sci. Tech. 50, 197–208.

Pyrz, R., 1994b. Correlation of microstructure variability and local stress field in two-phase materials. Mater. Sci. Engrg. A177, 253–259.

Raghavan, P., Ghosh, S., 2004. Concurrent multi-scale analysis of elastic composites by a multi-level computational model. Comput. Methods Appl. Mech. Engrg. 193, 497–538.

Raghavan, P., Ghosh, S., 2004. Adaptive multi-scale computational modeling of composite materials. Comput. Mod. Engrg. Sci. 5 (2), 151–170.

Raghavan, P., Moorthy, S., Ghosh, S., Pagano, N.J., 2001. Revisiting the composite laminate problem with an adaptive multi-level computational model. Comput. Sci. Tech. 61, 1017–1040.

Simo, J.C., Ju, J.W., 1987. Strain and stress-based continuum damage models, Part I: Formulation. Int. J. Solids Struct. 23 (7), 821–840.

Talreja, R., 1990. In: Boehler, J.P. (Ed.), Internal Variable Damage Mechanics of Composite Materials, Yielding, Damage and Failure of Anisotropic Solids, EGF5. Mechanical Engineering Publications, pp. 509–533.

Talreja, R., 1991. Continuum modeling of damage in ceramic matrix composites. Mech. Mater. 12, 165–180.

Tsai, S.W., Wu, E.M., 1971. General theory of strength for anisotropic materials. J. Comput. Mater. 5, 58–80.

Tvergaard, V., 1995. Fiber debonding and breakage in a whisker reinforced metal. Mater. Sci. Engrg. A 90, 215–222.

Voyiadjis, G.Z., Kattan, P.I., 1999. Advances in Damage Mechanics: Metals and Metal Matrix Composites. Elsevier.

Yuan, F.G., Pagano, N.J., Cai, X., 1997. Elastic moduli of brittle matrix composites with interfacial debonding. Int. J. Solids Struct. 34 (2), 177–201.

Zhu, Y.Y., Cescotto, S., 1995. A fully coupled elasto-visco-plastic damage theory for anisotropic materials. Int. J. Solids Struct 32 (11), 1607–1641.